Mechanics of Advanced Materials and Structures

ISSN: (Print) (Online) Journal homepage: www.tandfonline.com/journals/umcm20

Slope stability/instability analysis of advanced nanocomposite reinforced column structure under mechanical loading via coupled Carrera unified formulation, layer-wise and Laplace transform approaches

Xiaoshan Xu, Gongxing Yan, M. Atif & Mohammed El-Meligy

To cite this article: Xiaoshan Xu, Gongxing Yan, M. Atif & Mohammed El-Meligy (05 Nov 2024): Slope stability/instability analysis of advanced nanocomposite reinforced column structure under mechanical loading via coupled Carrera unified formulation, layer-wise and Laplace transform approaches, Mechanics of Advanced Materials and Structures, DOI: 10.1080/15376494.2024.2416470

To link to this article: https://doi.org/10.1080/15376494.2024.2416470

Published online: 05 Nov 2024.

MECHANICS OF ADVANCED MATERIALS AND STRUCTURES
https://doi.org/10.1080/15376494.2024.2416470

Taylor & Francis
Taylor & Francis Group

ORIGINAL ARTICLE

Slope stability/instability analysis of advanced nanocomposite reinforced column structure under mechanical loading via coupled Carrera unified formulation, layer-wise and Laplace transform approaches

Xiaoshan Xu[a], Gongxing Yan[b,c], M. Atif[d], and Mohammed El-Meligy[e,f]

[a]College of Civil Engineering, Chongqing Vocational Institute of Engineering, Chongqing, China; [b]School of Intelligent Construction, Luzhou Vocational and Technical College, Luzhou, Sichuan, China; [c]Luzhou Key Laboratory of Intelligent Construction and Low-carbon Technology, Luzhou, China; [d]Department of Physics and Astronomy, College of Science, King Saud University, Riyadh, Saudi Arabia; [e]Jadara University Research Center, Jadara University, Jordan; [f]Applied Science Research Center, Applied Science Private University, Amman, Jordan

ABSTRACT

This study presents a comprehensive investigation into the slope stability and instability of column structures made of Triply Periodic Minimal Surfaces (TPMS) under mechanical loading. TPMS structures, known for their high strength-to-weight ratio, are increasingly used in engineering applications, particularly in lightweight structures. However, their stability behavior under complex loading conditions remains largely unexplored. To address this gap, we employ a coupled approach integrating the Carrera Unified Formulation (CUF), the Layer-Wise (LW) theory, and Laplace Transform techniques. The CUF framework, known for its versatility in modeling structural behavior across different geometrical and loading configurations, is utilized to capture the mechanical response of the TPMS-based columns. The LW theory further enhances the model by accurately representing the through-thickness behavior, particularly crucial for layered or composite TPMS structures. Finally, the Laplace Transform approach is applied to efficiently solve the governing differential equations, reducing the computational complexity of time-dependent mechanical analyses. A parametric study investigates the influence of various geometrical parameters, material properties, and loading conditions on the stability of the structures. The results highlight the critical factors influencing slope stability, including the interplay between the TPMS geometry and material distribution. Moreover, the findings offer insights into failure mechanisms, providing a basis for optimizing the design of TPMS-based columns for enhanced mechanical performance. This work contributes to advancing the theoretical understanding of TPMS structures, offering novel methodologies for slope stability analysis in complex mechanical systems.

ARTICLE HISTORY
Received 24 September 2024
Accepted 9 October 2024

KEYWORDS
Slope stability; triply periodic minimal surfaces (TPMS); Carrera unified formulation; layer-wise theory; mechanical loading

1. Introduction

Composite structures are vital in modern engineering due to their unique combination of lightweight properties and high strength, making them indispensable in various industries [1–4]. Composites, typically made from reinforcing fibers such as carbon, glass, or aramid embedded in a matrix material like epoxy, provide engineers with the ability to design structures that meet stringent performance criteria without the weight penalty of traditional materials like steel or aluminum [5]. One of the most significant advantages of composite materials is their high strength-to-weight ratio, which is critical in applications like aerospace, automotive, and marine industries [6–8]. By reducing the weight of structures, engineers can improve fuel efficiency, payload capacity, and overall performance. For instance, the aerospace industry relies heavily on composites for manufacturing aircraft wings, fuselages, and other components, reducing weight and improving fuel economy. Composites also offer excellent corrosion resistance, which extends the lifespan of structures in harsh environments, such as chemical plants, offshore platforms, and bridges [9]. Unlike metals, composites do not rust or degrade as easily, leading to lower maintenance costs and longer service life [10]. This makes them particularly appealing for engineers designing structures that must withstand environmental stressors over extended periods. Another key benefit is the tailorability of composites [11, 12]. Engineers can optimize the orientation and type of fibers to achieve desired mechanical properties for specific applications, allowing for greater control over the behavior of the structure under various loads [13]. This flexibility is not possible with traditional isotropic materials, where properties are uniform in all directions. Composites also excel in vibration damping, which is crucial in applications like automotive suspensions, wind turbine blades, and sports equipment [14]. By absorbing and dissipating energy, composites help reduce noise, improve ride comfort, and extend the life of components subjected to dynamic loads [15]. The anisotropic nature of composites—where properties differ along different directions—allows engineers to strategically place materials only where they are needed, optimizing material usage and minimizing unnecessary weight [16]. This enables innovative

CONTACT Gongxing Yan yaaangx@126.com School of Intelligent Construction, Luzhou Vocational and Technical College, Luzhou, Sichuan, China.

design possibilities, like the creation of complex geometries or integrating multiple functions into a single component [17]. In addition to mechanical benefits, composites contribute to thermal stability in industries where materials are exposed to extreme temperatures. They have low thermal conductivity, making them ideal for applications in space structures, satellites, and electronics, where temperature fluctuations can cause material failure [18]. Furthermore, composite structures are crucial for sustainability efforts [19]. As industries aim to reduce their environmental footprint, the use of composites can contribute to greener solutions by reducing fuel consumption and emissions in transportation sectors [20]. Additionally, many composites can be made from renewable or recyclable materials, aligning with global sustainability goals [21]. Lastly, the long-term cost savings associated with composite materials, due to their durability, low maintenance, and ability to outperform traditional materials in extreme conditions, make them an attractive choice for engineers [22]. Although the initial cost of composites can be higher, their overall lifecycle cost is often lower, especially in applications requiring long-term durability and performance [23]. In summary, composite structures offer engineers a versatile, high-performance material option that is well-suited to meet the growing demands of modern engineering applications, ranging from aerospace to civil infrastructure, thanks to their customizable, durable, and lightweight properties [24].

The Carrera Unified Formulation (CUF) is a significant advancement in the field of structural modeling, offering engineers a powerful tool to analyze complex structures with enhanced accuracy and efficiency [25]. It provides a unified framework that simplifies the implementation of different structural theories, such as classical beam, plate, and shell theories, as well as more advanced models [26]. One of its core benefits is its ability to handle a wide variety of structural configurations, from simple to multilayered composites, using a single formulation approach [27]. CUF is particularly valuable in the analysis of structures with varying geometries and material properties, such as aerospace, automotive, and civil engineering applications [28]. Engineers can seamlessly switch between different levels of model fidelity—ranging from basic one-dimensional to advanced three-dimensional formulations—depending on the complexity of the structure and the required accuracy [29]. This adaptability makes CUF highly efficient, especially in optimizing computational resources during finite element analysis. In addition, CUF supports higher-order theories without the need for complex mathematical formulations, enabling more accurate predictions of phenomena such as vibration, buckling, and dynamic response [30]. The formulation is also well-suited for analyzing laminated composite materials, which are increasingly used in modern engineering structures due to their superior strength-to-weight ratios [28]. Moreover, CUF's versatility allows engineers to easily incorporate various boundary conditions, loading scenarios, and material nonlinearity, enhancing its applicability in real-world structural analysis. Its unified nature eliminates the need for problem-specific formulations, significantly reducing development time and simplifying code implementation [29]. This capability is essential for industries where precision and efficiency are critical, allowing engineers to perform detailed structural analysis while minimizing errors [31]. Overall, the Carrera Unified Formulation offers a flexible, accurate, and computationally efficient approach to structural modeling, making it an indispensable tool for engineers tackling complex design and analysis challenges [32].

Numerical investigation plays a crucial role in modern engineering due to its ability to analyze complex systems that are difficult or impossible to solve analytically [33, 34]. By using numerical methods, engineers can simulate real-world phenomena with high precision, providing insights into the behavior of structures, materials, and systems under various conditions [35, 36]. It allows for the evaluation of different design alternatives before physical prototypes are created, saving both time and resources [37, 38]. Numerical analysis is particularly important in fields like aerospace, civil, and mechanical engineering, where precision is critical for safety and performance [39, 40]. In the design of bridges, buildings, and vehicles, for instance, numerical methods can predict load distribution, stress concentrations, and failure points [41, 42]. The outputs of the previous references can be used as the input in Refs. [43, 44]. These insights help engineers optimize designs for strength, durability, and cost-effectiveness [45, 46]. Moreover, numerical simulations enable the study of phenomena such as fluid dynamics, heat transfer, and electromagnetic fields, which are often too complex for purely experimental investigation [47, 48]. By applying methods like finite element analysis (FEA) and computational fluid dynamics (CFD), engineers can refine their designs with confidence [49, 50]. Additionally, numerical investigations provide a framework for integrating multidisciplinary considerations, such as material science and environmental factors, into the design process [51, 52]. This comprehensive approach ensures that products and structures meet both performance standards and regulatory requirements [53, 54]. The outputs of the previous references can be used as the input in Refs. [55, 56]. Engineers can also use numerical tools to investigate the effects of nonlinearities, uncertainties, and dynamic loads, which are vital for assessing long-term performance and safety [57, 58]. Ultimately, numerical methods offer a cost-effective, efficient, and flexible approach for tackling a wide range of engineering challenges, making them indispensable in both academic research and industry [59, 60]. Ref. [61] aimed to improve economic stability by implementing targeted financial strategies and risk management techniques. This was achieved by using advanced algorithms to classify credit card users based on their financial behaviors. In contrast, Ref. [62] utilizes extreme value theory in conjunction with mixture models to effectively identify and evaluate tail risks in financial markets, estimating the probability of rare but significant financial losses.

The slope stability and instability of column structures composed of triply periodic minimal surfaces under mechanical stress are thoroughly examined in this work. Because of its excellent strength-to-weight ratio, TPMS structures are being used more and more in engineering applications, especially for lightweight constructions. Their stability behavior under intricate loading situations, however, is yet mostly unknown. We use a linked method that integrates the Layer-Wise theory, the Carrera Unified Formulation, and Laplace Transform techniques in order to close this gap. To capture the mechanical reaction of the TPMS-based columns, the CUF framework—which is well-known for its adaptability in simulating structural behavior across various geometrical and loading configurations—is used. By faithfully capturing the through-thickness behavior, which is especially important for layered or composite TPMS structures, the LW theory improves the model even more. Ultimately, time-dependent mechanical studies' computing complexity is decreased by effectively solving the governing differential equations using the Laplace Transform method. The impact of different geometrical factors, material characteristics, and loading circumstances on the stability of the constructions is examined using a parametric research. The findings draw attention to the important variables affecting slope stability, such as the interaction between the material distribution and TPMS shape. Furthermore, the results provide light on the reasons of failure and serve as a foundation for improving the mechanical performance of TPMS-based column designs. This study offers new approaches for slope stability analysis in complicated mechanical systems, furthering our theoretical knowledge of TPMS structures.

2. Mathematical modeling

When it comes to the other two orthogonal dimensions, a column's longitudinal length (L) is fundamental. A beam is a typical thin construction. The global coordinate system for the column structure, where the $x-z$ plane and $y-$ axis ($0 \le y \le L$) are perpendicular and parallel to the cross section, respectively, is adopted to be the Cartesian coordinate system, as seen in Figure 1.

2.1. TPMS architectures

Three uniform sheet-based models and their 3D printing prototypes are taken into consideration in order to streamline the design process for TPMS substrates. These models are Primitive (P), Gyroid (G), and I-graph and wrapped package-graph (IWP), as shown in Figure 2. The effective elastic parameters of TPMS-based cellular material models, namely Poisson's ratio, shear modulus, and Young's modulus, must be approximated in order to forecast their mechanical behavior with any degree of accuracy. Using a two-phase fitting approach, a recent effective homogenization strategy of three distinct cellular TPMS forms (P, G, and IWP) is suggested [51]. Therefore, the relative density $\rho = \rho(z)/\rho_s$, where $\rho(z)$ and ρ_s, respectively, reflect the mass density of TPMS and the base material, may be used to describe the material characteristics of various TPMS structures. These are the precise formulae for these amounts [63].

$$\frac{E}{E_s} = \begin{cases} C_1^E \rho^{n_1^E}, & \rho \le k_E \\ C_2^E \rho^{n_2^E} + C_3^E, & \rho > k_E \end{cases}, \tag{1a}$$

$$\frac{G}{G_s} = \begin{cases} C_1^G \rho^{n_1^G}, & \rho \le k_G \\ C_2^G \rho^{n_2^G} + C_3^G, & \rho > k_G \end{cases}, \tag{1b}$$

$$\nu = \begin{cases} a_1 e^{(b_1 \rho)} + d_1, & \rho \le k_\nu \\ a_2 \rho^2 + b_2 \rho + d_2, & \rho > k_\nu \end{cases}. \tag{1c}$$

As demonstrated in Eqs. (1a)–(1c), it is clear to see that 12 parameters are required to fully determine the material properties for each TPMS architecture. These coefficients are provided in Table 1 and Eqs. (2a) and (2b) [63].

$$C_1^E (k_E)^{n_1^E} = C_2^E (k_E)^{n_2^E} + C_3^E, C_3^E = 1 - C_2^E, \tag{2a}$$

$$d_1 = \nu_s - a_1 e^{b_1 k_\nu}, b_2 = -a_2(k_\nu + 1), d_2 = \nu_s - a_2 - b_2. \tag{2b}$$

On the other hand, we assume that the porosity distribution of the TPMS substrate layer is mathematically determined using two mass density functional grading distributions as follows [51]

$$\rho(z) = \rho_s \rho_{\max}[1 - \rho_0 + \rho_0 \psi(z)], \tag{3}$$

where $\psi(z)$ represents the distribution function and is explicitly expressed as follows

$$\psi(z): \begin{cases} PA: \psi_1(z) = \left(\frac{z}{h} + \frac{1}{2}\right)^{n_A} \\ PB: \psi_2(z) = \left[1 - \cos\left(\frac{\pi z}{h}\right)\right]^{n_S} \end{cases}, \tag{4}$$

in which h is the thickness of the microplates; $\rho_0 = 1 - \rho_{\min}/\rho_{\max}$ represents the porosity parameter, with $\rho_{\min}$ and $\rho_{\max}$ respectively denoting the minimum and maximum values of the relative density. Additionally, the definitions of the power indexes n_A and n_S can be found in the Appendix section.

In this study, a straight single-walled carbon nanotube (SWCNT) reinforcement phase is added to improve the cellular TPMS substrate layer. It is widely known that the agglomeration phenomenon, which happens during synthesis under realistic circumstances, has a major impact on the reinforcing performance of composite materials. Because of this, the CNT-reinforced base material is described in this work using a two-factor model, which takes into consideration the agglomeration processes suggested by Shi et al. [64]. In this model, SWCNTs are dispersed randomly

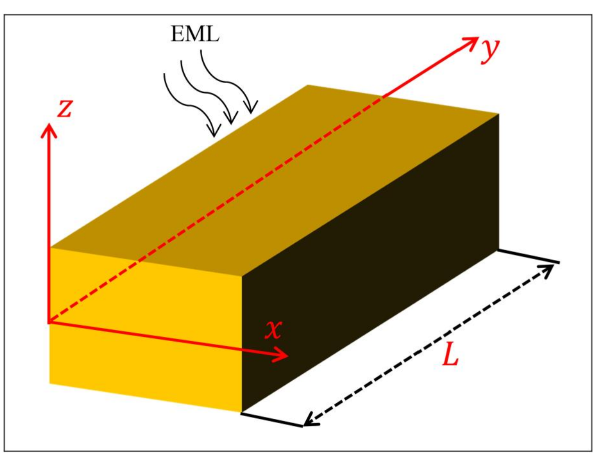

Figure 1. The geometry of the column structure under external mechanical loading (EML) and global coordinate system.

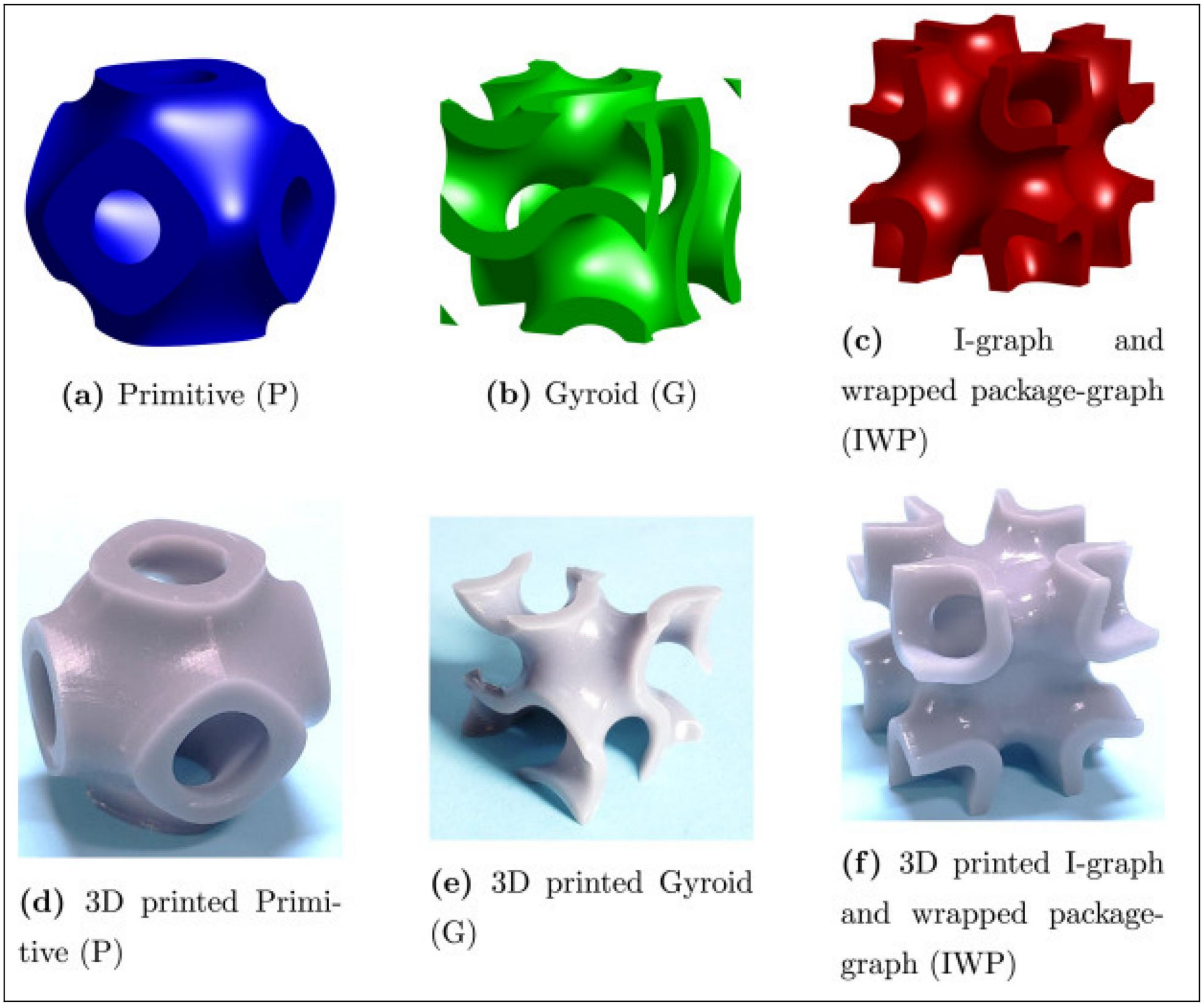

Figure 2. Various porous TPMS structures [59].

Table 1. Twelve coefficients for determining the material characteristics of TPMS types.

		TPMS type		
Property	Parameter	P	G	IWP
Elastic modulus, E (GPa)	C_1^E	0.317	0.596	0.597
	n_1^E	1.264	1.467	1.225
	n_2^E	2.006	2.351	1.782
	k_m^E	0.25	0.45	0.35
Shear modulus, G (GPa)	C_1^G	0.705	0.777	0.529
	n_1^G	1.189	1.544	1.287
	n_2^G	1.715	1.982	2.188
	k_m^G	0.25	0.45	0.35
Poisson's ratio, ν	a_1	0.314	0.192	2.597
	b_1	−1.004	−1.349	−0.157
	a_2	0.152	0.402	0.201
	k_ν	0.55	0.50	0.13

throughout the material, with a few areas designated as "agglomeration regions" that may have larger concentrations of CNTs. Three model parameters are defined as follows: $\mathcal{V}_r$ (volume fraction of CNT reinforcement), ξ (agglomeration ratio), and ζ (agglomeration CNT reinforcement ratio).

$$\mathcal{V}_r = \frac{V_r}{V}, \xi = \frac{V^{aggl}}{V}, \zeta = \frac{V_r^{aggl}}{V_r}, \tag{5}$$

where V, V^{aggl}, V_r, and V_r^{aggl} stand for the volume of the total material, total CNT reinforcement, and CNT reinforcement, in that order. The Appendix section defines the agglomeration phenomena as well as the effective mechanical characteristics of composite materials. Furthermore, using the mixing rule, the mass density of the CNTR material is calculated as follows.

$$\rho_s = \rho_m \mathrm{V}_m + \rho_r \mathrm{V}_r. \tag{6}$$

where the mass densities of the matrix and CNT are denoted by ρ_m and ρ_r, respectively. The matrix's volume fraction is $\mathrm{V}_m = 1 - \mathrm{V}_r$.

2.2. Carrera unified formulation (CUF)

At a given position in the structure, the displacement vector $\mathbf{u}(x, y, z; t)$, strain vector $\boldsymbol{\epsilon}(x, y, z; t)$, and stress vector $\boldsymbol{\sigma}(x, y, z; t)$ may be represented as follows:

$$\mathbf{u}(x,y,z;t)=\{u\ v\ w\}^{\mathrm{T}},\tag{7a}$$

$$\boldsymbol{\epsilon}(x,y,z;t)=\{\epsilon_{yy}\epsilon_{xx}\epsilon_{zz}\epsilon_{xz}\epsilon_{yz}\epsilon_{xy}\}^{\mathrm{T}},\tag{7b}$$

$$\boldsymbol{\sigma}(x,y,z;t)=\{\sigma_{yy}\sigma_{xx}\sigma_{zz}\sigma_{xz}\sigma_{yz}\sigma_{xy}\}^{\mathrm{T}}.\tag{7c}$$

where superscript "T" is the transpose operator. t is the time variable, being omitted in the remaining part for convenience. The constitutive equations follow Hooke's law, while the geometrical equations satisfy the linear relation:

$$\boldsymbol{\epsilon}(x,y,z)=\mathbf{D}\mathbf{u}(x,y,z),\tag{8a}$$

$$\boldsymbol{\sigma}(x,y,z)=\mathbf{C}\boldsymbol{\epsilon}(x,y,z).\tag{8b}$$

where C is the material coefficient matrix and D is a 6×3 differential operator matrix. The references [13] may be seen in their explicit forms. Well-known for their ability to analyze the mechanics of thin, isotropic structures with bending-dominated deformation are classical column models like EBBM and TBM. However, because of the weaker cross-section kinematic fields, these theories are not as often used in the modeling of thin-walled and composite structures. In order to solve this issue, CUF creates a unified column model in which any function pertaining to x and z coordinates may be used to generate the cross-section kinematic fields, as in the following example:

$$\mathbf{u}(x,y,z)=F_\tau(x,z)\mathbf{u}_\tau(y),\tau=1,2,\ldots,M\tag{9}$$

where the 1D generalized displacement vector along the column's axis is denoted by $\mathbf{u}_\tau(y)$. The arbitrary cross-section expansion, $F_\tau(x,z)$, establishes the kind of column model. M is the number of expansion terms, and τ is the summation in the repeated index.

2.3. Hierarchical Legendre expansions (HLE)

Initially, Szabó et al. [65] used hierarchical Legendre polynomials to produce p-version FEM. The CUF-Hierarchical Legendre Expansions (HLE) column model was created by Carrera et al. [66] using hierarchical Legendre polynomials as $F_\tau(x,z)$. This work served as inspiration for their work. Layer-wise kinematics are naturally enabled in CUF-HLE since the polynomials are specified on the local natural coordinate system and transferred into the global coordinate system *via* the isoparametric transformation. Three groups comprise the formulation of 2D Legendre polynomials: internal, side, and vertex functions. Specifically, in order to produce the first-order expansions, which are bilinear Lagrange polynomials, vertice functions are introduced:

$$F_\tau=\frac{1}{4}(1+rr_\tau)(1+ss_\tau),\tau=1,2,3,4\tag{10}$$

Thus, in the natural coordinate system, r_τ and s_τ are the coordinates of four vertexes across the quadrilateral area. Over the span $[-1,+1]$, r and s change.

$$F_\tau(r,s)=\frac{1}{2}(1-s)\phi_j(r),\tau=5,9,13,18,\ldots\tag{11a}$$

$$F_\tau(r,s)=\frac{1}{2}(1+r)\phi_j(s),\tau=6,10,14,19,\ldots\tag{11b}$$

$$F_\tau(r,s)=\frac{1}{2}(1+s)\phi_j(s),\tau=7,11,15,20,\ldots\tag{11c}$$

$$F_\tau(r,s)=\frac{1}{2}(1-s)\phi_j(s),\tau=8,12,16,21,\ldots\tag{11d}$$

where $\phi_j(r)$ indicates $1D$ Legendre internal functions, see Ref. [67] for further information. For $j>4$, the higher-order cross-section kinematics must be supplemented by a set of internal functions. The main distortion emerges from inside and disappears from the periphery. Typically, the jth-order expansions have $j-3$ internal functions. Their statements may be expressed succinctly as follows:

$$F_\tau(r,s)=\phi_j(r)\phi_k(s),j,k\geq2;\tau=17,22,23,28,29,30,\ldots\tag{12}$$

According to the preceding formulations, all of the lower-order kinematics—that is, the vertex, side, and internal functions—are included in the whole higher-order kinematics ($j\geq4$), which can explain all rational deformations. The structural theory is generated *via* Legendre-based interpolating functions, which results in pure displacements and higher-order modes as the model's degrees of freedom.

3. Governing equations

The governing equations of a generic column structure in a Cartesian reference frame can be derived *via* the variational principle of virtual work. For static, free vibration and dynamic response analyses they hold:

$$\delta L_{\mathrm{int}}=\delta L_{\mathrm{ext}},\tag{13a}$$

$$\delta L_{\mathrm{int}}=-\delta L_{\mathrm{ine}},\tag{13b}$$

$$\delta L_{\mathrm{int}}=\delta L_{\mathrm{ext}}-\delta L_{\mathrm{ine}}.\tag{13c}$$

where δ denotes the symbol of the virtual variation. L_{int} is the strain energy, L_{ine} indicates the inertial work, L_{ext} represents the work done by the external force.

3.1. Stiffness matrix

The virtual variation of strain energy can be written as:

$$\delta L_{\mathrm{int}}=\int_V\delta\boldsymbol{\epsilon}^{\mathrm{T}}\boldsymbol{\sigma}\mathrm{d}V,\tag{14}$$

where V is the volume.

Consider the geometrical relations and constitutive law under the assumption of small displacements, rotations and deformations, as follows:

$$\boldsymbol{\epsilon}=\mathbf{D}\mathbf{u},\tag{15a}$$

$$\boldsymbol{\sigma}=\mathbf{C}\boldsymbol{\epsilon}.\tag{15b}$$

where $\mathbf{D}$ is 6×3 differential operator matrices. $\mathbf{C}$ is 6×6 stiffness matrices of the material. The explicit formulations of $\mathbf{D}$ and $\mathbf{C}$ have already been reported in the literature [68].

By substituting geometrical and constitutive equations in Eqs. (8a) and (b) and the displacement assumption in Eq. (9) into Eq. (14), one has:

$$\delta L_{\text{int}} = (\delta \mathbf{q}_{sj})^{\mathrm{T}} \int_V R_j^p F_s \mathbf{D}^{\mathrm{T}} \mathbf{C} \mathbf{D} F_\tau R_i^p \mathrm{d}V \delta \mathbf{q}_{\tau i} = (\delta \mathbf{q}_{sj})^{\mathrm{T}} \mathbf{K}_e^{\tau sij} \mathbf{q}_{\tau i}. \tag{16}$$

where $\mathbf{K}_e^{\tau sij}$ is the fundamental nucleus of the element stiffness matrix, which is composed of 3×3 matrices.

$$\mathbf{K}_e^{\tau sij} = \begin{bmatrix} K_{e(11)}^{\tau sij} & K_{e(12)}^{\tau sij} & K_{e(13)}^{\tau sij} \\ K_{e(21)}^{\tau sij} & K_{e(22)}^{\tau sij} & K_{e(23)}^{\tau sij} \\ K_{e(31)}^{\tau sij} & K_{e(32)}^{\tau sij} & K_{e(33)}^{\tau sij} \end{bmatrix}. \tag{17}$$

In the case of laminated structures with orthotropic material, their explicit formulations are given in Appendix A.

$$\begin{aligned} K_{e(11)}^{\tau sij} = {} & J_{i,yj} \triangleleft F_\tau C_{46} F_{s,z} \triangleright + J_{i,yj} \triangleleft F_\tau C_{26} F_{s,x} \triangleright + J_{i,yj,y} \triangleleft F_\tau C_{66} F_s \\ & \triangleright + J_{ij} \triangleleft F_{\tau,z} C_{44} F_{s,z} \triangleright + J_{ij} \triangleleft F_{\tau,z} C_{24} F_{s,x} \triangleright + J_{ij,y} \\ & \triangleleft F_{\tau,z} C_{46} F_s \triangleright + J_{ij,y} \triangleleft F_{\tau,x} C_{26} F_s \triangleright + J_{ij} \triangleleft F_{\tau,x} C_{24} F_{s,z} \\ & \triangleright + J_{ij} \triangleleft F_{\tau,x} C_{22} F_{s,x} \triangleright , \end{aligned} \tag{18a}$$

$$\begin{aligned} K_{e(12)}^{\tau sij} = {} & J_{i,yj} \triangleleft F_\tau C_{66} F_{s,x} \triangleright + J_{i,yj} \triangleleft F_\tau C_{56} F_{s,z} \triangleright + J_{i,yj,y} \triangleleft F_\tau C_{36} F_s \\ & \triangleright + J_{ij} \triangleleft F_{\tau,x} C_{26} F_{s,x} \triangleright + J_{ij} \triangleleft F_{\tau,x} C_{25} F_{s,z} \triangleright + J_{ij} \\ & \triangleleft F_{\tau,z} C_{46} F_{s,x} \triangleright + J_{ij} \triangleleft F_{\tau,z} C_{45} F_{s,z} \triangleright + J_{ij,y} \triangleleft F_{\tau,z} C_{34} F_s \\ & \triangleright + J_{ij,y} \triangleleft F_{\tau,x} C_{23} F_s \triangleright , \end{aligned} \tag{18b}$$

$$\begin{aligned} K_{e(13)}^{\tau sij} = {} & J_{i,yj} \triangleleft F_\tau C_{46} F_{s,x} \triangleright + {}_{i,yj} \triangleleft F_\tau C_{16} F_{s,z} \triangleright + J_{i,yj,y} \triangleleft F_\tau C_{56} F_s \\ & \triangleright + J_{ij} \triangleleft F_{\tau,z} C_{44} F_{s,x} \triangleright + J_{ij} \triangleleft F_{\tau,z} C_{14} F_{s,z} \triangleright + J_{ij} \\ & \triangleleft F_{\tau,x} C_{24} F_{s,x} \triangleright + J_{ij} \triangleleft F_{\tau,x} C_{12} F_{s,z} \triangleright + J_{ij,y} \triangleleft F_{\tau,z} C_{45} F_s \\ & \triangleright + J_{ij,y} \triangleleft F_{\tau,x} C_{25} F_s \triangleright , \end{aligned} \tag{18c}$$

$$\begin{aligned} K_{e(21)}^{\tau sij} = {} & J_{ij,y} \triangleleft F_{\tau,x} C_{66} F_s \triangleright + J_{ij,y} \triangleleft F_{\tau,z} C_{56} F_s \triangleright + J_{i,yj} \triangleleft F_\tau C_{34} F_{s,z} \\ & \triangleright + J_{i,yj} \triangleleft F_\tau C_{23} F_{s,x} \triangleright + J_{i,yj,y} \triangleleft F_\tau C_{36} F_s \triangleright + J_{ij} \\ & \triangleleft F_{\tau,x} C_{46} F_{s,x} \triangleright + J_{ij} \triangleleft F_{\tau,x} C_{26} F_{s,x} \triangleright + J_{ij} \triangleleft F_{\tau,z} C_{45} F_{s,z} \\ & \triangleright + J_{ij} \triangleleft F_{\tau,z} C_{25} F_{s,x} \triangleright , \end{aligned} \tag{18d}$$

$$\begin{aligned} K_{e(22)}^{\tau sij} = {} & J_{ij} \triangleleft F_{\tau,x} C_{66} F_{s,x} \triangleright + J_{ij} \triangleleft F_{\tau,x} C_{56} F_{s,z} \triangleright + J_{ij} \triangleleft F_{\tau,z} C_{56} F_{s,x} \\ & \triangleright + J_{ij} \triangleleft F_{\tau,z} C_{55} F_{s,z} \triangleright + J_{ij,y} \triangleleft F_{\tau,x} C_{36} F_s \triangleright + J_{ij,y} \\ & \triangleleft F_{\tau,z} C_{35} F_s \triangleright + J_{i,yj} \triangleleft F_\tau C_{36} F_{s,x} \triangleright + J_{i,yj} \triangleleft F_\tau C_{35} F_{s,z} \\ & \triangleright + J_{i,yj,y} \triangleleft F_\tau C_{33} F_s \triangleright , \end{aligned} \tag{18e}$$

$$\begin{aligned} K_{e(23)}^{\tau sij} = {} & J_{ij} \triangleleft F_{\tau,x} C_{46} F_{s,x} \triangleright + J_{ij} \triangleleft F_{\tau,x} C_{16} F_{s,z} \triangleright + J_{ij} \triangleleft F_{\tau,z} C_{45} F_{s,x} \\ & \triangleright + J_{ij} \triangleleft F_{\tau,z} C_{15} F_{s,z} \triangleright + J_{ij,y} \triangleleft F_{\tau,x} C_{56} F_s \triangleright + J_{ij,y} \\ & \triangleleft F_{\tau,z} C_{55} F_s \triangleright + J_{i,yj} \triangleleft F_\tau C_{34} F_{s,x} \triangleright + J_{i,yj} \triangleleft F_\tau C_{13} F_{s,z} \\ & \triangleright + J_{i,yj,y} \triangleleft F_\tau C_{35} F_s \triangleright , \end{aligned} \tag{18f}$$

$$\begin{aligned} K_{e(31)}^{\tau sij} = {} & J_{i,yj} \triangleleft F_\tau C_{45} F_{s,z} \triangleright + J_{i,yj} \triangleleft F_\tau C_{25} F_{s,x} \triangleright + J_{i,yj,y} \triangleleft F_\tau C_{56} F_s \\ & \triangleright + J_{ij} \triangleleft F_{\tau,x} C_{44} F_{s,z} \triangleright + J_{ij} \triangleleft F_{\tau,x} C_{24} F_{s,x} \triangleright + J_{ij} \\ & \triangleleft F_{\tau,z} C_{12} F_{s,x} \triangleright + J_{ij} \triangleleft F_{\tau,z} C_{14} F_{s,z} \triangleright + J_{ij,y} \triangleleft F_{\tau,x} C_{46} F_s \\ & \triangleright + J_{ij,y} \triangleleft F_{\tau,z} C_{16} F_s \triangleright , \end{aligned} \tag{18g}$$

$$\begin{aligned} K_{e(32)}^{\tau sij} = {} & J_{i,yj} \triangleleft F_\tau C_{56} F_{s,x} \triangleright + J_{i,yj} \triangleleft F_\tau C_{55} F_{s,z} \triangleright + J_{i,yj,y} \triangleleft F_\tau C_{35} F_s \\ & \triangleright + J_{ij} \triangleleft F_{\tau,z} C_{16} F_{s,x} \triangleright + J_{ij} \triangleleft F_{\tau,z} C_{15} F_{s,z} \triangleright + J_{ij} \\ & \triangleleft F_{\tau,x} C_{46} F_{s,x} \triangleright + J_{ij} \triangleleft F_{\tau,x} C_{45} F_{s,z} \triangleright + J_{ij,y} \triangleleft F_{\tau,x} C_{34} F_s \\ & \triangleright + J_{ij,y} \triangleleft F_{\tau,z} C_{13} F_s \triangleright , \end{aligned} \tag{18h}$$

$$\begin{aligned} K_{e(33)}^{\tau sij} = {} & J_{i,yj} \triangleleft F_\tau C_{45} F_{s,x} \triangleright + J_{i,yj} \triangleleft F_\tau C_{15} F_{s,z} \triangleright + J_{i,yj,y} \triangleleft F_\tau C_{55} F_s \\ & \triangleright + J_{ij} \triangleleft F_{\tau,x} C_{44} F_{s,x} \triangleright + J_{ij} \triangleleft F_{\tau,x} C_{14} F_{s,z} \triangleright + J_{ij} \\ & \triangleleft F_{\tau,z} C_{14} F_{s,x} \triangleright + J_{ij} \triangleleft F_{\tau,z} C_{11} F_{s,z} \triangleright + J_{ij,y} \triangleleft F_{\tau,x} C_{45} F_s \\ & \triangleright + J_{ij,y} \triangleleft F_{\tau,z} C_{15} F_s \triangleright , \end{aligned} \tag{18i}$$

where $\triangleleft \cdot \triangleright = \int_\Omega \mathrm{d}\Omega$ is a cross-section moment parameter, whereas

$$J_{ij} = \int_0^1 R_i^p R_j^p y,_\xi \mathrm{d}\xi, \tag{19a}$$

$$J_{ij,y} = \int_0^1 R_i^p R_{j,\xi}^p \mathrm{d}\xi, \tag{19b}$$

$$J_{i,yj} = \int_0^1 R_{i,\xi}^p R^p \mathrm{d}\xi, \tag{19c}$$

$$J_{i,yj,y} = \int_0^1 R_{i,\xi}^p R_{j,\xi}^p / y,_\xi \mathrm{d}\xi. \tag{19d}$$

and "derivatives" is indicated by the suffix after the comma. Note that the aforementioned integration is carried out over the parametric space [0, 1]. As expounded in Ref. [69], the mathematical transformation of integration variables provides an alternate method for doing Gauss quadrature smoothly. Changing the column model and shape function types does not change the elements of the basic nucleus in the element stiffness matrix. According to this sort of invariance, the global stiffness matrix of any type of column model may be easily built by adjusting the loop statements that are represented by the code's indices τ, s, i, and j properly.

4. B-spline functions

This study is innovative in that it approximates $u_\tau(y)$ using B-spline functions. The form function of the resultant element in the setting of IGA is contrasted with that of the traditional FEM element after a short introduction to the fundamentals of B-spline functions. The following is the recursive definition of these functions at beginning order $p = 0$ using the piece-wise constant representation:

$$N_i^0(\xi) = \begin{cases} 1 \ \ if \ \ \xi_i \le \xi \le \xi_{i+1} \\ 0 \ \ otherwise \end{cases}. \tag{20}$$

where ξ_i stands for the ith knot.

For $p = 1, 2, 3, \ldots,$ one obtains:

$$N_i^p(\xi) = \frac{\xi - \xi_i}{\xi_{i+p} - \xi_i} N_i^{p-1}(\xi) + \frac{\xi_{i+p+1} - \xi}{\xi_{i+p+1} - \xi_{i+1}} N_{i+1}^{p-1}(\xi). \tag{21}$$

where both N_i^0 and N_i^p are B-spline functions and p corresponds to the order.

Usually, the knot vector includes a sequence of non-decreasing coordinates in the parametric space, written as:

$$\Xi = \{\xi_1, \xi_2, \ldots, \xi_{n+p+1}\}. \tag{22}$$

where n is the number of functions. The knot vector, also known as uniform or non-uniform B-splines, may have a uniform or non-uniform distribution in the parametric space. Unlike Lagrange interpolation functions, this allows several knots to share a single value. This characteristic will influence the B-spline functions' continuity $(C^1, C^2, \ldots, C^\infty)$. The knot vector is referred to as the open one, or endpoints interpolation, for the given order p if the first and final knots occur $p + 1$ times. On the other hand, the knot vector possesses C^{p-m} continuous derivatives at that place if the multiplicity of the internal knot is m. As a result, the B-spline functions may exactly create the basic straight line as follows:

$$y = \sum_{i=1}^{n} N_i^p(\xi) y_i. \tag{23}$$

where y_i is the coordinate of the control point, which may fall off the curve.

Through the definition above, $u_\tau(y)$ in Eq. (9) can be approximated by the weighted linear combination of $N_i^p(\xi)$. By substitution of this approximation into Eq. (9), one can obtain:

$$\mathbf{u}(x, y, z) = F_\tau(x, z) N_i^p(\xi) \mathbf{q}_{\tau i}, \tau = 1, 2, \ldots, M \ \ i = 1, 2, \ldots, n \tag{24}$$

where weighted coefficient $\mathbf{q}_{\tau i}$ is the generalized nodal displacement vector, the subscript τ implies the summation. Corresponding B-spline elements may be created using the displacement pattern mentioned above; this process is comparable to that used in the FEM. To increase the analytical accuracy, the initial coarse meshes—which fall into three categories: $h-$, $p-$, and $k-$ types—should be gently refined. In this study, only the h-type will be used, and its mechanism is based on inserting the knot into the knot vector without altering the function's order or the geometric form. Those who are interested might see Hughes et al. [70] for information on the other two categories.

4.1. Loading vector

The work performed by the external force in the case of the concentrated load $\mathbf{F} = \{F_x, F_y, F_z\}$ operating at the position (x_c, y_c, z_c) is stated as follows:

$$\delta L_{\text{ext}} = \delta \mathbf{u}^{\text{T}} \mathbf{F}. \tag{25}$$

Analogously, other kinds of loading conditions, such surface and line loads, may be handled. When Eq. (24) is substituted for Eq. (25), the result is:

$$\delta L_{ext} = \delta \mathbf{q}_{sj}^{\text{T}} F_s R_j^p \mathbf{F} = \delta \mathbf{q}_{sj}^{\text{T}} \mathbf{P}_e^{sj}. \tag{26}$$

where F_s and R_j^p are evaluated at the corresponding position (x_c, z_c) and (y_c), $\mathbf{P}_e^{sj}$ is the element nodal load vector.

4.2. Mass matrix

The virtual variation of inertial work can be expressed [71]:

$$\delta L_{\text{ine}} = \int_V \delta \mathbf{u}_s^{\text{T}} \rho \ddot{\mathbf{u}}_\tau \text{d}V. \tag{27}$$

where superimposed dots denote the second derivative with respect to time, substituting Eq. (24) into Eq. (27), it holds:

$$\delta L_{\text{ine}} = \int_V \delta \mathbf{q}_{sj}^{\text{T}} (J_{ij} \triangleleft \rho F_\tau F_s \triangleright) \mathbf{I}) \ddot{\mathbf{q}}_{\tau i} \text{d}V = \delta \mathbf{q}_{sj}^{\text{T}} \mathbf{M}_e^{\tau sij} \ddot{\mathbf{q}}_{\tau i}. \tag{28}$$

where symbols J_{ij} and $\triangleleft \cdot \triangleright$ can be found in Appendix A, I is a 3×3 identity matrix. $\mathbf{M}_e^{\tau sij}$ is the element mass matrix.

4.3. Algebraic expressions of governing equations

The static analysis inquiries into the equilibrium between internal and external forces. Considering Eqs. (16) and (13a), the final algebraic system of governing equations as proposed in Eq. (13a) is obtained

$$\mathbf{Kq} = \mathbf{P}. \tag{29}$$

The balance between elastic and inertial forces is examined by the free vibration analysis. In this problem, the notion of virtual displacements is articulated as previously explained in Sections 4.1 and 4.3.

$$\mathbf{K}\mathbf{q} + \mathbf{M}\ddot{\mathbf{q}} = 0. \tag{30}$$

The solution of q may be found by multiplying the motion's amplitude function (Q) by the function linked to natural frequency (ω)-, $e^{i\omega t}$, when harmonic motion is considered. Therefore, it is possible to reduce Eq. (31) to a standard eigenvalue problem:

$$(\mathbf{K} - \omega^2\mathbf{M})\mathbf{Q} = 0. \tag{31}$$

In the more broad scenario, the dynamic issue takes into consideration the contributions of internal, external, and inertial energy. Consequently, the set of governing equations in algebraic form becomes

$$\mathbf{K}\mathbf{q} + \mathbf{M}\ddot{\mathbf{q}} = \mathbf{P}. \tag{32}$$

Applying Laplace transform [72] to Eq. (32) brings about the following relations

$$\mathbf{K}\hat{\mathbf{q}} + \mathbf{M}S^2\hat{\mathbf{q}} = \hat{\mathbf{P}}. \tag{33}$$

The layer-wise method combined with the Laplace transform to Eq. (33), allows for the determination of the displacement for each layer. Using the modified formulation of Dubner and Abate, the displacements are produced over time by using the inverse Laplace transform [72]. Therefore, Eq. (34) is the formula that was used in this investigation to carry out the inverse Laplace transform.

$$\zeta(t) = \frac{2e^{at}}{T}\left[-\frac{A_0}{2} + \sum_{k=0}^{\infty}\left(A_k\cos\left(\frac{2k\pi t}{T}\right) - B_k\sin\left(\frac{2k\pi t}{T}\right)\right)\right], \tag{34}$$

Here

$$A_0 = Re[F(a)], A_k = Re\left[F\left(a + i\frac{2k\pi}{T}\right)\right], \quad B_k = Im\left[F\left(a + i\frac{2k\pi}{T}\right)\right], \tag{35a}$$

$$S = a + i\frac{2k\pi}{T}, aT = 5. \tag{35b}$$

5. Results and discussion

5.1. Validation

The simply supported (SS) square beam with $L/b = 10$ exhibits the first seven non-dimensional flexural frequencies, $\omega^* = (\omega L^2/b)\sqrt{\rho/E}$, in Table 1. The current LE models' findings are contrasted with reference FE results from Refs. [73, 74], as well as those from traditional theories (EBBM, TBM), CUF(TE)-DSM, and CUF(LE)-Navier theory. A range of LE models are taken into account in the table shown in Figure 3. The accuracy of the current strong form LE beam is shown by the comparison of the data in Table 2. It even shows convergence with regard to EBBM in the case of the simplest one, 1L4. The Navier solution, which also makes use of the LE model, and the results produced by the current technique coincide rather well. It is important to take note of 1×2L4 and 2×1L4, since they are distinct models with varying flexure directions along ox and oz. Despite having the same amount of degrees of freedom as 1L9, the 2×2L4 model in Figure 3(d) yields somewhat better accurate results, at least when compared to the lower frequencies. The 1L16 model's findings demonstrate its superior accuracy and higher-order, fourth-order interpolation capabilities, which are especially noticeable in the higher frequency range.

Table 2 presents the first seven non-dimensional flexural frequencies for a simply supported (SS) square beam with a length-to-breadth ratio ($L/b = 10$). Various models and methods are used to calculate these frequencies, illustrating differences in results based on different approaches. The TBM-DSM and EBBM-DSM models, as referenced in [74],

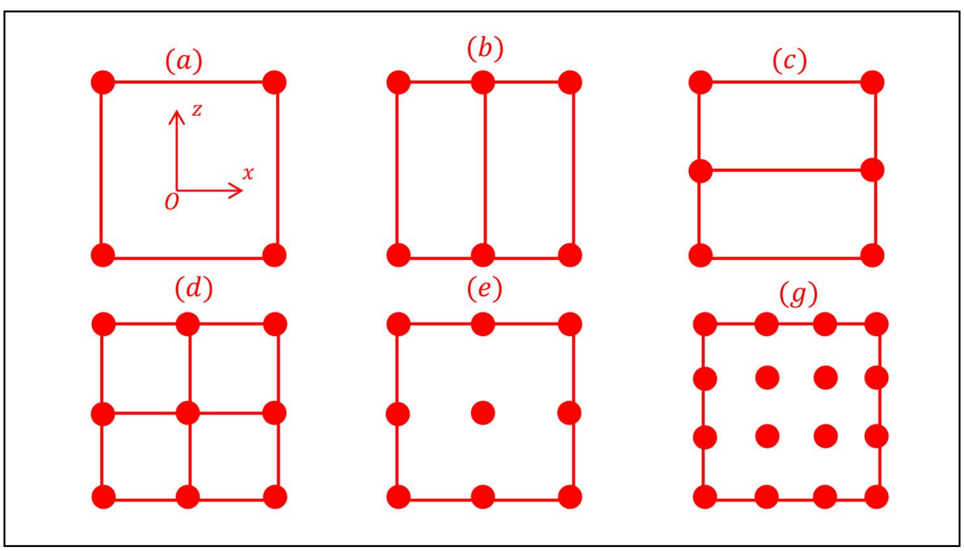

Figure 3. LE modeling of the square cross-section beam. (a) 1L4. (b) 1×2L4. (c) 2×1L4. (d) 2×2L4. (e) 1L9. (f) 1L16.

Table 2. First seven non-dimensional flexural frequencies $\omega^* = (\omega L^2/b)\sqrt{\rho/E}$ for the simply supported (SS) square beam, $L/b = 10$.

Model	1	2	3	4	5	6	7
TBM-DSM [1]	2.807	10.779	22.849	37.858	54.856	73.192	92.334
EBBM-DSM [1]	2.838	11.213	24.742	42.847	64.869	90.330	117.859
FEM [74]							
NAS1D50	2.813	10.841	23.055	38.225	55.256	73.331	91.907
NAS1D100	2.813	10.841	23.060	38.246	55.323	73.491	92.225
NAS1D200	2.813	10.842	23.062	38.254	55.340	73.532	92.296
CUF (TE)-DSM [74]							
$N = 3$	2.803	10.723	22.621	37.299	53.812	71.509	89.963
$N = 4$	2.803	10.722	22.617	37.282	53.765	71.402	89.759
CUF (LE)-Navier [73]							
1L4	3.063	11.704	24.653	40.573	58.415	77.456	97.226
1×2L4	2.914	11.168	23.617	39.030	56.416	75.074	94.536
2×1L4	2.998	11.474	24.213	39.923	57.575	76.452	96.083
2×2L4	2.839	10.890	23.055	38.143	55.187	73.500	92.621
1L9	2.808	10.784	22.869	37.902	54.929	73.268	92.453
1L16	2.803	10.722	22.618	37.291	53.794	71.472	89.898
Current theory							
1L4	3.064	11.707	24.657	40.572	58.418	77.459	97.224
1×2L4	2.915	11.169	23.619	39.032	56.421	75.077	94.538
2×1L4	2.999	11.477	24.214	39.926	57.574	76.453	96.085
2×2L4	2.844	10.891	23.056	38.146	55.189	73.504	92.624
1L9	2.809	10.785	22.870	37.905	54.926	73.267	92.456
1L16	2.806	10.723	22.619	37.293	53.797	71.474	89.897

provide results that serve as baseline comparisons. The first frequency for TBM-DSM is 2.807, increasing to 92.334 for the seventh frequency. In comparison, the EBBM-DSM shows slightly higher values, with the first frequency at 2.838 and the seventh at 117.859, indicating higher stiffness predictions from this model. Results obtained using the FEM [74] are also included, with three variations based on the number of elements (NAS1D50, NAS1D100, and NAS1D200). The frequencies increase with more refined element numbers, demonstrating the impact of mesh refinement on the accuracy of the results. For example, NAS1D200 yields slightly higher values than NAS1D50, with the first frequency increasing from 2.813 to 2.813, and the seventh from 91.907 to 92.226, respectively. The CUF (TE)-DSM model with $N = 3$ and $N = 4$ [74] shows close agreement with the DSM-based models. As expected, increasing the polynomial order from $N = 3$ to $N = 4$ does not drastically affect the results, with the frequencies remaining nearly constant, e.g. the first frequency for both is 2.803, and the seventh is approximately 89.863. The CUF (LE)-Navier [73] model introduces different configurations (e.g. 1L4, 2×2L4), showing variability in the predicted frequencies. For instance, the first frequency for 1L4 is 3.063, which is higher than that of other models, suggesting a stiffer response prediction. The seventh frequency for this method, at 97.226, also deviates from other methods, reflecting differences in how boundary conditions and assumptions affect the flexural frequencies. The current theory, presented at the bottom of the table, offers results for the same configurations. The first frequency for 1L4 is 3.063, consistent with the CUF (LE)-Navier model. The rest of the frequencies closely align, with the seventh frequency at 97.225, confirming the consistency between the models. This table highlights the influence of different modeling techniques, boundary conditions, and element refinements on predicting flexural frequencies in square beams. From Table 2 can be concluded that there is good agreement between the current work and those of published articles.

5.2. Parametric result

Figure 4 appears to illustrate the dynamic response of a column structure composed of advanced nanocomposite reinforced materials designed with different Triply Periodic Minimal Surface (TPMS) architectures—Primitive, Gyroid, and IWP (Schwarz P) models—under mechanical loading. The graphs aim to compare the slope stability/instability of these structures based on their deformation characteristics. The top graph presents a time series of the slope's rate of change, $\partial w/\partial x$, for each TPMS architecture. The x-axis represents time (in seconds), while the y-axis denotes the change in slope rate, potentially indicating the magnitude of deformation or stress along the column's length. The three curves—red for Primitive, blue for Gyroid, and black for IWP—show oscillatory behavior, typical of dynamic systems under mechanical excitation. The amplitude and frequency of the oscillations differ for each architecture, suggesting that each TPMS model responds differently to mechanical stress. This difference in behavior could highlight varying levels of stiffness or internal stress distribution across the materials, with the Gyroid (blue) showing larger oscillations compared to the other models. This suggests greater sensitivity or susceptibility to mechanical instability. The bottom two subplots (b and c) offer phase-plane diagrams, where the x-axis represents $\frac{\partial^2 w}{\partial x \partial t}$ (rate of slope change), and the y-axis represents $\frac{\partial w}{\partial x}$ (curvature or second derivative of the slope). These diagrams visualize the dynamic stability of the system, with trajectories indicating the evolution of slope and curvature over time. In subplot (b), for $\frac{\partial^2 w}{\partial x \partial t}$ vs. $\frac{\partial w}{\partial x}$, the three TPMS architectures again show distinct behaviors. The red trajectory (Primitive) forms larger loops, while the blue (Gyroid) and black (IWP) show tighter loops. This suggests that the Primitive architecture experiences greater deformation but possibly returns to equilibrium more predictably, whereas the Gyroid and IWP have a more intricate stability profile. Subplot (c) focuses on the slope stability by looking at the $\frac{\partial^3 w}{\partial x \partial t^2}$ versus $\frac{\partial^2 w}{\partial x \partial t}$, capturing how the change in slope evolves with time. This further highlights the mechanical response diversity among the TPMS models. The overall analysis underscores that the Gyroid model shows more complexity and larger deformations, which could imply a greater potential for instability under prolonged mechanical loading, while the Primitive and IWP offer more predictable, albeit less stable, behavior.

Figure 5 illustrates the slope stability and instability analysis of a nanocomposite reinforced column structure under mechanical loading, considering different TPMS architectures with a PB distribution function. The three architectures compared are Primitive, Gyroid, and IWP (Schwarz P), with the same mechanical loading conditions, but now analyzed through the PB distribution. The top graph shows how the slope rate evolves over time for each of the TPMS models. The x-axis represents time (in seconds), while the y-

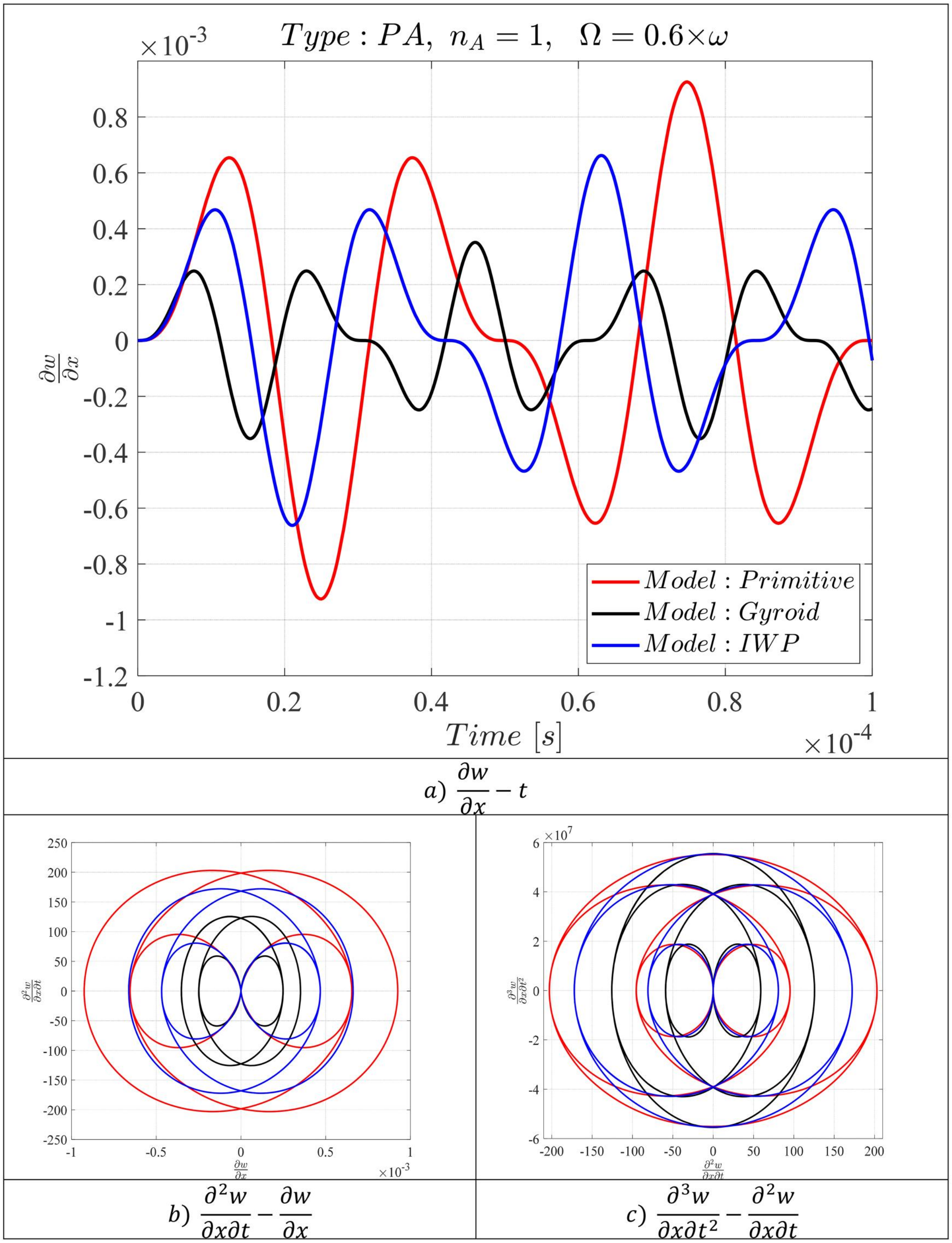

Figure 4. Slope stability/instability information of the advanced nanocomposite reinforced column structure under mechanical loading for various TPMS architectures and PA as the distribution function.

axis reflects the rate of slope change, $\frac{\partial w}{\partial x}$, in the structure. The red curve corresponds to the Primitive model, the blue curve represents the Gyroid, and the black curve stands for the IWP architecture. The oscillatory behavior of the structures is more pronounced here compared to Figure 4. The amplitudes are smaller, but the frequencies appear to be higher, indicating a potentially stiffer or more responsive system. The Primitive architecture (red) has the highest amplitudes, suggesting a larger deformation rate compared to Gyroid (blue) and IWP (black). The varying frequencies and amplitudes suggest distinct mechanical behaviors for each TPMS, with Primitive responding with larger oscillations, while the IWP and Gyroid show tighter, more controlled oscillations. In subplots (b) and (c), phase-plane diagrams further characterize the dynamic responses. In subplot (b), which compares the slope rate $\frac{\partial w}{\partial x}$ with the curvature $\frac{\partial^2 w}{\partial x \partial t}$, each TPMS architecture exhibits a different phase portrait. The Primitive architecture (red) forms larger and

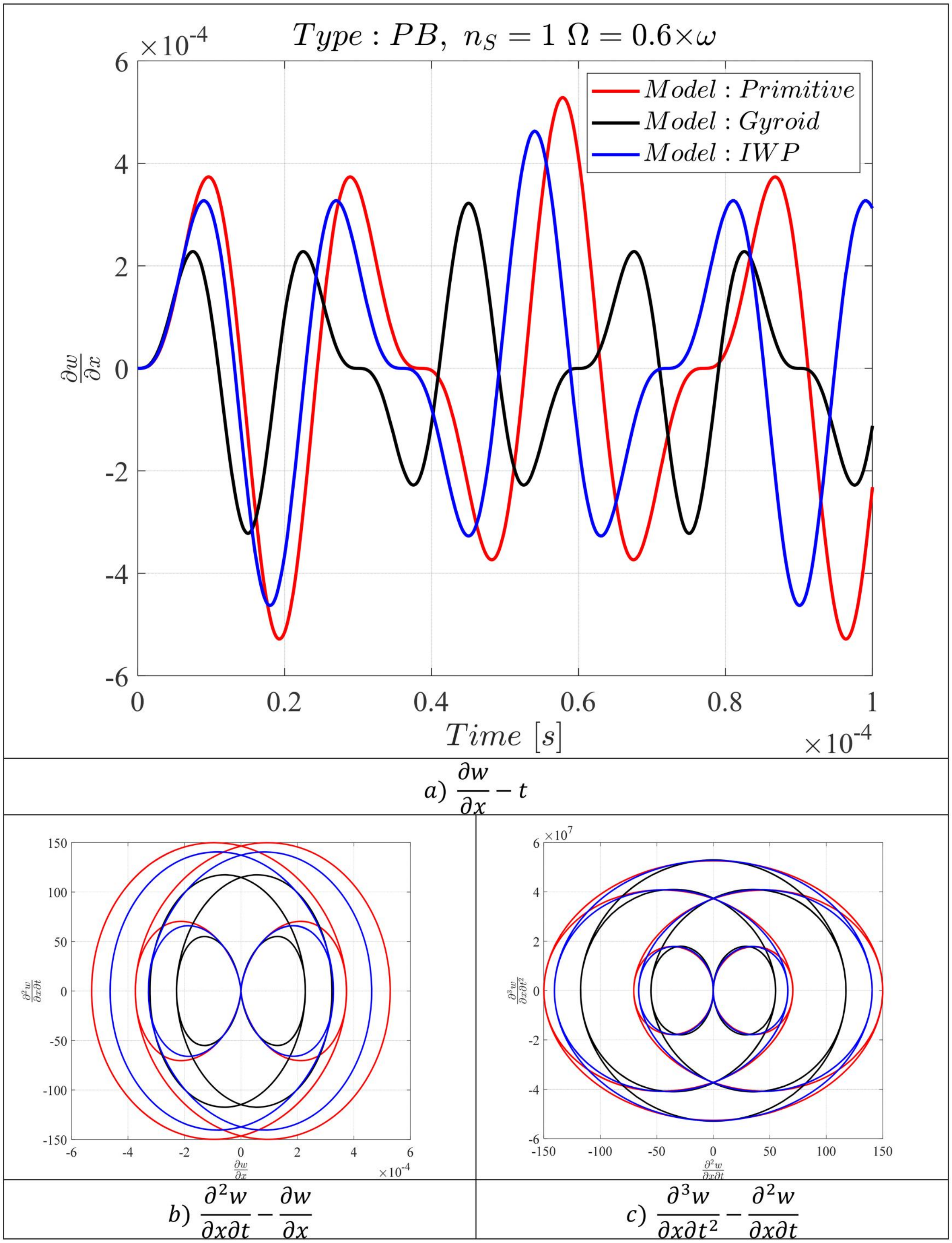

Figure 5. Slope stability/instability information of the advanced nanocomposite reinforced column structure under mechanical loading for various TPMS architectures and PB as the distribution function.

more elliptical loops, while the Gyroid (blue) and IWP (black) create more compact, cyclic paths. This shows that the Primitive model exhibits greater mechanical deformation but may stabilize back to equilibrium more effectively. The Gyroid, however, shows a more complex response with tighter loops, implying greater stiffness and potential instability over time. Subplot (c) compares $\frac{\partial^3 w}{\partial x \partial t^2}$ versus $\frac{\partial^2 w}{\partial x \partial t}$, depicting how the slope rate changes with time. The Primitive model (red) again shows larger loops, implying more substantial deformations, while the Gyroid and IWP form denser loops. The denser loops for the Gyroid suggest increased stability, but potentially more susceptibility to complex dynamic behavior due to its intricate surface structure. The IWP model demonstrates a middle ground, with more uniform and predictable dynamics compared to the other two models. Overall, Figure 5 demonstrates that the Primitive architecture exhibits larger deformation magnitudes but returns more predictably to equilibrium, while the

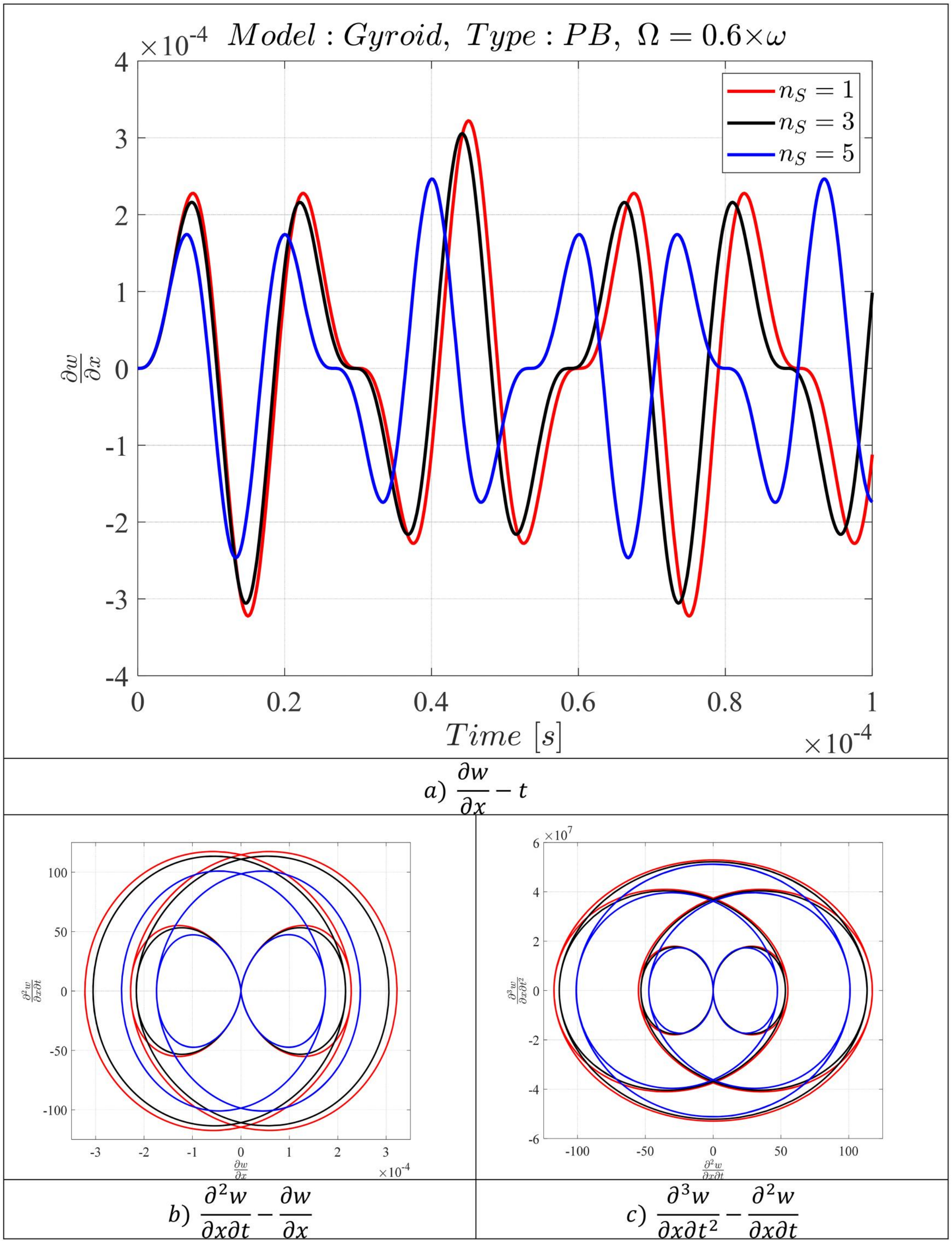

Figure 6. Slope stability/instability information of the advanced nanocomposite reinforced column structure under mechanical loading for various n_S and PB as the distribution function.

Gyroid and IWP models display more complex stability profiles. The smaller amplitude and higher frequency of oscillations for the PB distribution function may indicate a more rigid structure under mechanical loading conditions. However, the differences in dynamic response between the TPMS models emphasize the importance of choosing the appropriate architecture for specific mechanical performance needs.

Figure 6 demonstrates the slope stability and instability of a nanocomposite reinforced column structure under mechanical loading, focusing on the Gyroid architecture. The mechanical response is analyzed with varying values of n_S, representing different structural configurations within the PB distribution function. The values of n_S considered are 1, 3, and 5, denoted by red, blue, and black curves, respectively. In the top graph, the x-axis represents time (in seconds), while the y-axis shows the rate of slope change, $\frac{\partial w}{\partial x}$. The different colors illustrate the oscillatory response of the structure for the corresponding values of n_S. The red curve $n_S = 1$ exhibits the highest amplitude oscillations, while the blue curve ($n_S = 3$) and the black curve

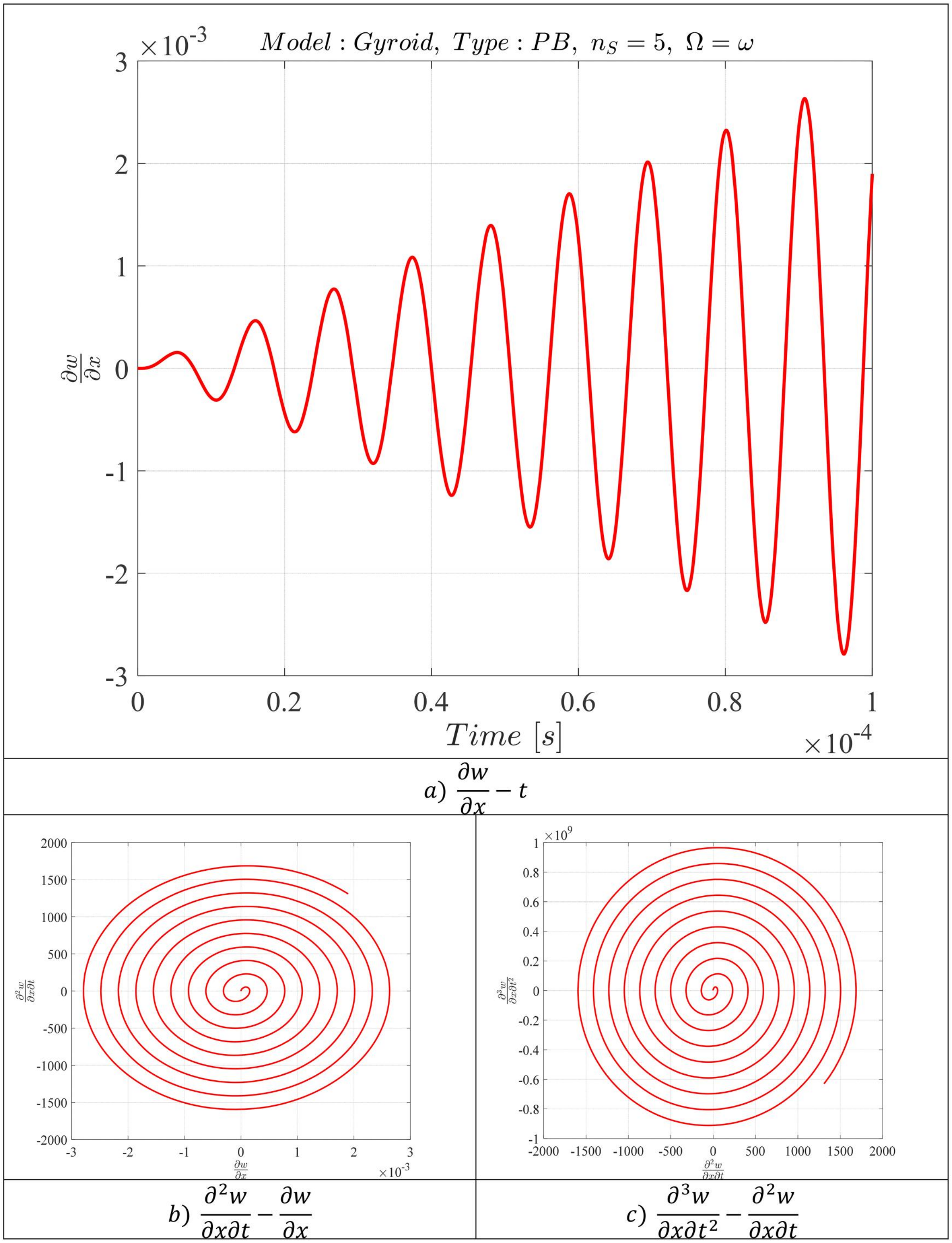

Figure 7. Slope stability/instability information of the advanced nanocomposite reinforced column structure under mechanical loading at various times.

($n_S = 5$) display progressively lower amplitudes. This indicates that as n_S increases, the mechanical response becomes less intense in terms of deformation rate, suggesting increased structural stability or reduced sensitivity to mechanical loading. Moreover, the oscillation frequencies seem to increase with higher n_S, indicating that the system becomes stiffer and responds more quickly to mechanical stress. The bottom two subplots (b and c) provide further insight through phase-plane diagrams. Subplot (b) plots $\frac{\partial^2 w}{\partial x \partial t}$ (slope rate) against $\frac{\partial w}{\partial x}$ (curvature or second derivative of the slope). The phase portraits reveal the dynamic behavior for each n_S value. The red curve ($n_S = 1$) forms larger loops, indicative of greater deformation, while the blue ($n_S = 3$) and black ($n_S = 5$) curves form tighter loops. This suggests that the structure experiences reduced deformation as n_S increases, likely resulting in higher stability and less susceptibility to large-scale mechanical oscillations. Subplot (c) presents the relationship between $\frac{\partial^3 w}{\partial x \partial t^2}$ and $\frac{\partial^2 w}{\partial x \partial t}$, illustrating how the slope rate evolves over time. The red curve ($n_S = 1$) again shows larger loops compared to the blue and black curves, indicating a more dynamic and less stable

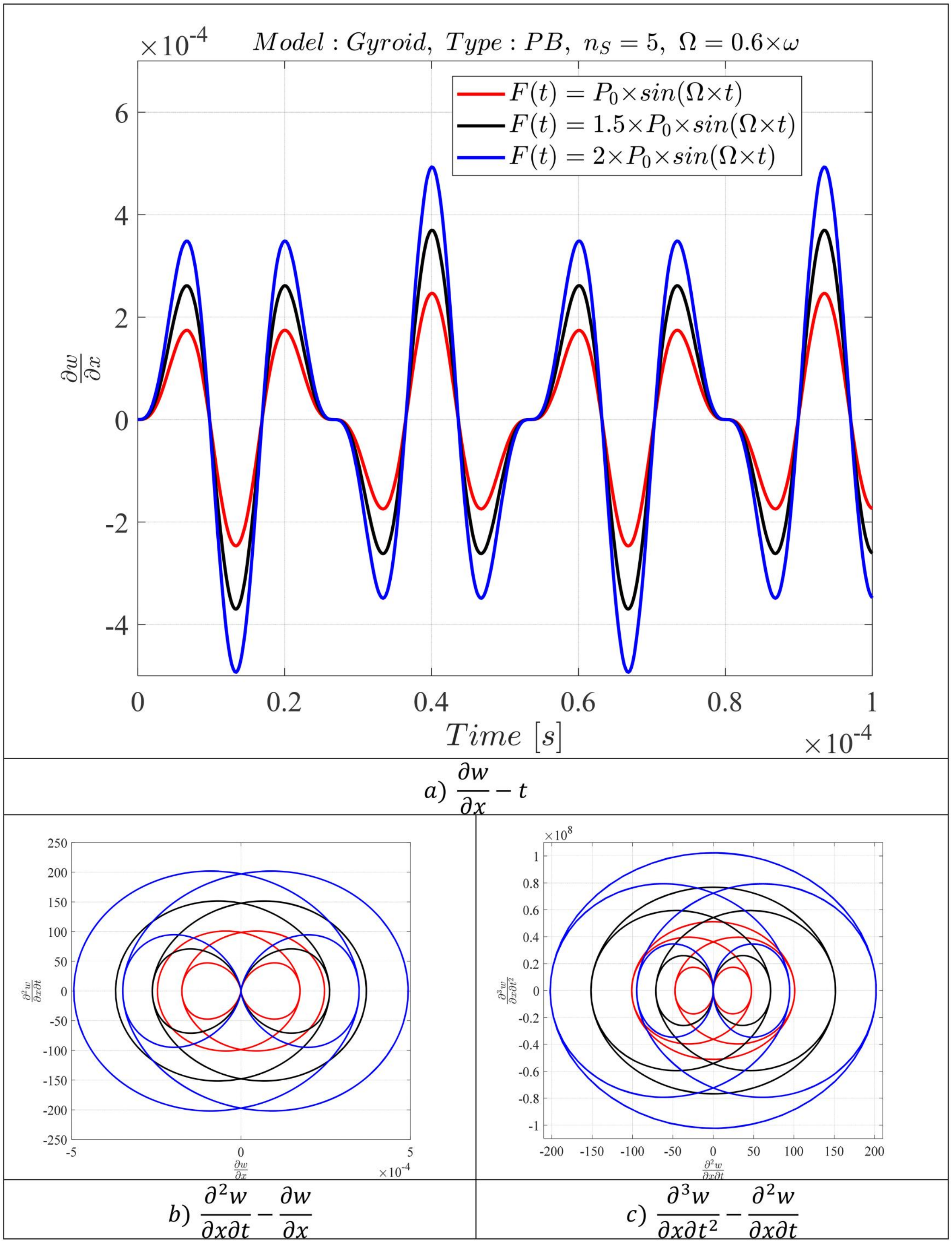

Figure 8. Slope stability/instability information of the advanced nanocomposite reinforced column structure for various distribution functions of mechanical loading.

response. The progressively smaller and more compact loops for ($n_S = 3$) and ($n_S = 5$) reinforce the observation that higher n_S values correspond to more controlled, stable behavior under mechanical loading. Overall, Figure 6 demonstrates that as n_S increases, the Gyroid-based structure becomes stiffer, exhibiting smaller deformations and a more stable dynamic response. This indicates that by tuning n_S, the mechanical performance of the column structure can be optimized for specific applications, with higher n_S values favoring greater stability and reduced mechanical instability under load.

Figure 7 presents a detailed analysis of slope stability and instability in an advanced nanocomposite reinforced column structure composed of Triply Periodic Minimal Surface materials under mechanical loading, specifically with a gyroid-based configuration. The figure illustrates the behavior of the structure over time in response to loading and highlights different aspects of the deformation and response dynamics. In Figure 7(a), the graph plots the time evolution of the slope derivative ($\partial w/\partial x$) as a function of time, indicating the dynamic response of the column structure under loading. The oscillatory nature of the curve suggests the structure undergoes significant fluctuations in response to the mechanical load. The increasing amplitude of oscillations over time implies a possible onset of instability, where the structure experiences larger deformations as time progresses. This time-varying behavior is characteristic of instability phenomena, such as flutter or dynamic buckling, often observed in slender structures or those with complex geometries like TPMS materials. The specific model used in this analysis, referred to as a gyroid with parameters $n_s = 5$ and $\Omega = \omega$, emphasizes the structural configuration and loading conditions employed. Figure 7(b,c) provide further insight into the slope variations in terms of phase-space trajectories, plotting $\frac{\partial^2 w}{\partial x \partial t}$ against $\partial w/\partial x$ at different instants. These phase diagrams reveal spiraling paths, which are a hallmark of a stable system that could approach a limit cycle, or indicate complex behavior like bifurcation points. The symmetrical and closed-loop trajectories in both subfigures reflect a system oscillating within a bounded range, suggesting some degree of stability, despite the oscillatory behavior observed in the time plot. These phase portraits are essential for understanding the equilibrium points and stability margins of the system. A tighter spiral (in Figure 7(b)) likely represents a period of relatively lower energy or small perturbations, while the broader loops (in Figure 7(c)) could signify increasing energy levels or transition toward instability. In summary, this figure offers a comprehensive depiction of the dynamic response of a TPMS-based column structure, showcasing both time-domain and phase-space analyses. The oscillatory trends, coupled with the evolving phase portraits, underscore the complexity of stability behavior in such advanced materials under mechanical stress.

Figure 8 presents an analysis of the slope stability and instability of a nanocomposite-reinforced column structure with a gyroidal configuration, subjected to different forms of mechanical loading. This study focuses on the behavior of the structure under various loading distributions characterized by functions $F(t) = P_0 \sin(\Omega t)$, $F(t) = 1.5 P_0 \sin(\Omega t)$, and $F(t) = 2 P_0 \sin(\Omega t)$. These loading distributions introduce different levels of force, as depicted by the increasing factors of P_0, ranging from standard (red curve), intermediate (black curve), to higher force (blue curve). In Figure 8(a), the graph shows the time evolution of the slope derivative ($\partial w/\partial x$) over time for each of the loading distributions. The red curve corresponds to the smallest loading function, while the black and blue curves correspond to increased load levels. The behavior under the smallest loading is relatively stable with moderate oscillations, but as the loading function increases (e.g. the blue curve), the amplitude of the oscillations grows significantly. This suggests that the higher the mechanical load applied to the structure, the more prone the column is to experience larger deformations, which could lead to instability. The oscillations seen in this figure can be interpreted as the structure's response to dynamic loads, with increasing energy leading to more pronounced deformations as the load grows. Figure 8(b,c) further analyze the system by presenting phase portraits, where $\frac{\partial^2 w}{\partial x \partial t}$ is plotted against $\partial w/\partial x$, for different instants of time. These phase-space diagrams give a clear representation of the system's stability under varying mechanical loads. In Figure 8(b), which corresponds to the lowest load (red curve), the closed, elliptical trajectories indicate a relatively stable state with small perturbations, suggesting that the structure can maintain its equilibrium without drastic changes. However, as seen in Figure 8(c), when the mechanical load increases (black and blue curves), the trajectories spread out into larger loops, indicating more complex oscillatory behavior and a higher tendency toward instability. The larger phase portraits indicate that the system is experiencing greater fluctuations, moving further from equilibrium as the mechanical load increases. In summary, Figure 8 provides critical insight into how different mechanical load distributions affect the slope stability of the gyroid-based nanocomposite column structure. As the mechanical load increases, the column becomes more unstable, which is reflected in both the time evolution of slope oscillations and the increasingly complex phase-space trajectories. These findings are vital for understanding how varying force distributions influence the overall stability of such advanced materials under dynamic mechanical conditions.

6. Conclusion

In this study, we analyzed the slope stability and instability of column structures made of TPMS under mechanical loading using a coupled approach that integrated the Carrera unified formulation, the layer-wise theory, and Laplace Transform techniques. The primary objective was to understand the stability behavior of TPMS structures, which had not been thoroughly explored in previous research, especially under complex loading conditions. We successfully employed the CUF, which provided a versatile and robust framework to model the mechanical response of TPMS columns with various geometrical and material configurations. By using the LW theory, we were able to account for the detailed through-thickness behavior of the structures, which was particularly relevant for multilayered TPMS or composite designs. The Laplace Transform further allowed us to efficiently solve the governing equations in the time domain, reducing computational demands and improving solution accuracy. The results of the parametric study revealed that the stability of TPMS columns was highly dependent on several critical factors, including their geometrical configuration, the material distribution within the structure, and the nature of the applied mechanical loading. We found that certain TPMS geometries exhibited enhanced stability due to their unique surface properties and load-distribution characteristics. Additionally, the interaction between different material layers in layered TPMS columns played a significant role in determining their overall stability or susceptibility to failure. In terms of instability, our analysis identified specific loading conditions and structural configurations that led to slope failure. These findings provided insight into the failure mechanisms of TPMS-based columns, enabling us to suggest design strategies for improving their mechanical performance. Overall, our work contributed to a deeper understanding of the slope stability and instability of TPMS structures, offering novel methodologies that can be applied to the design and optimization of lightweight, high-performance columns in engineering applications. This study laid the groundwork for future research into the stability of advanced periodic structures under mechanical loads.

Acknowledgments

The authors extend their appreciation to King Saud University, Saudi Arabia for funding this work through Researchers Supporting Project number (RSP2024R397), King Saud University, Riyadh, Saudi Arabia.

Disclosure statement

No potential conflict of interest was reported by the authors.

References

[1] M. Burkov, and A. Eremin, Evaluation of fracture toughness of hybrid CNT/CFRP composites, Mech. Adv. Mater. Struct., vol. 30, no. 14, pp. 2872–2881, 2023. DOI: 10.1080/15376494.2022.2064569.

[2] K. Katagiri, S. Honda, T. Okumura, S. Yamaguchi, S. Kawakita, K. Kume, and K. Sasaki, Enhancement method of CFRP with the non-hydrophobized cellulose nanofibers using aqueous electrodeposition solution, Mech. Adv. Mater. Struct., vol. 29, no. 26, pp. 4631–4638, 2022. DOI: 10.1080/15376494.2021.1934760.

[3] J. Purnomo, A. Han, R. Yamakawa, and B.S. Gan, Systematic calibration procedure for CFRP sheets and rods strengthened RC T-beams by using RBSM, Mech. Adv. Mater. Struct., vol. 30, no. 9, pp. 1913–1929, 2023. DOI: 10.1080/15376494.2022.2111483.

[4] F.J. Rescalvo, C. Timbolmas, R. Bravo, M. Portela, and J. Lorenzana, Multi-side digital image correlation (DIC) evaluation of CFRP bonded to poplar timber, Mech. Adv. Mater. Struct., vol. 31, no. 15, pp. 3367–3376, 2024. DOI: 10.1080/15376494.2023.2175396.

[5] G.M. Chen, J.F. Chen, and J.G. Teng, Behaviour of FRP-to-concrete interfaces between two adjacent cracks: a numerical investigation on the effect of bondline damage, Constr. Build. Mater., vol. 28, no. 1, pp. 584–591, 2012. DOI: 10.1016/j.conbuildmat.2011.08.074.

[6] Z. Li, W. Ma, H. Zhu, G. Deng, L. Hou, P. Xu, and S. Yao, Energy absorption prediction and optimization of corrugation-reinforced multicell square tubes based on machine learning, Mech. Adv. Mater. Struct., vol. 29, no. 26, pp. 5511–5529, 2022. DOI: 10.1080/15376494.2021.1958032.

[7] T.-T. Le, Practical machine learning-based prediction model for axial capacity of square CFST columns, Mech. Adv. Mater. Struct., vol. 29, no. 12, pp. 1782–1797, 2022. DOI: 10.1080/15376494.2020.1839608.

[8] G. Zhang, L. Tang, Z. Liu, L. Zhou, Y. Liu, and Z. Jiang, Machine-learning-based damage identification methods with features derived from moving principal component analysis, Mech. Adv. Mater. Struct., vol. 27, no. 21, pp. 1789–1802, 2020. DOI: 10.1080/15376494.2019.1710308.

[9] M.M. Abdel-Mottaleb, A. Mohamed, S.A. Karim, T.A. Osman, and A. Khattab, Preparation, characterization, and mechanical properties of polyacrylonitrile (PAN)/graphene oxide (GO) nanofibers, Mech. Adv. Mater. Struct., vol. 27, no. 4, pp. 346–351, 2020. DOI: 10.1080/15376494.2018.1473535.

[10] M.H. Amini, M. Soleimani, A. Altafi, and A. Rastgoo, Effects of geometric nonlinearity on free and forced vibration analysis of moderately thick annular functionally graded plate, Mech. Adv. Mater. Struct., vol. 20, no. 9, pp. 709–720, 2013. DOI: 10.1080/15376494.2012.676711.

[11] A.A. Daikh, and A.M. Zenkour, Effect of porosity on the bending analysis of various functionally graded sandwich plates, Mater. Res. Express., vol. 6, no. 6, p. 065703, 2019. DOI: 10.1088/2053-1591/ab0971.

[12] A.M. Zenkour, A quasi-3D refined theory for functionally graded single-layered and sandwich plates with porosities, Compos. Struct., vol. 201, pp. 38–48, 2018. DOI: 10.1016/j.compstruct.2018.05.147.

[13] E. Carrera, G. Giunta, and M. Petrolo, Beam Structures: Classical and Advanced Theories, John Wiley & Sons, 2011.

[14] H.-T. Thai, T.-K. Nguyen, T.P. Vo, and J. Lee, Analysis of functionally graded sandwich plates using a new first-order shear deformation theory, Eur. J. Mech. A Solids., vol. 45, pp. 211–225, 2014. DOI: 10.1016/j.euromechsol.2013.12.008.

[15] T.-K. Nguyen, V.-H. Nguyen, T. Chau-Dinh, T.P. Vo, and H. Nguyen-Xuan, Static and vibration analysis of isotropic and functionally graded sandwich plates using an edge-based MITC3 finite elements, Compos. B Eng., vol. 107, pp. 162–173, 2016. DOI: 10.1016/j.compositesb.2016.09.058.

[16] A. Tounsi, M.S.A. Houari, S. Benyoucef, and E.A. Adda Bedia, A refined trigonometric shear deformation theory for thermoelastic bending of functionally graded sandwich plates, Aerosp. Sci. Technol., vol. 24, no. 1, pp. 209–220, 2013. DOI: 10.1016/j.ast.2011.11.009.

[17] F.Z. Zaoui, D. Ouinas, and A. Tounsi, New 2D and quasi-3D shear deformation theories for free vibration of functionally graded plates on elastic foundations, Compos. B Eng., vol. 159, pp. 231–247, 2019. DOI: 10.1016/j.compositesb.2018.09.051.

[18] S.A. Farzam-Rad, B. Hassani, and A. Karamodin, Isogeometric analysis of functionally graded plates using a new quasi-3D shear deformation theory based on physical neutral surface, Compos. B Eng., vol. 108, pp. 174–189, 2017. DOI: 10.1016/j.compositesb.2016.09.029.

[19] Q.-H. Pham, T.T. Tran, and P.-C. Nguyen, Dynamic response of functionally graded porous-core sandwich plates subjected to blast load using ES-MITC3 element, Compos. Struct., vol. 309, p. 116722, 2023. DOI: 10.1016/j.compstruct.2023.116722.

[20] V.-L. Nguyen, M.-T. Tran, S. Limkatanyu, and J. Rungamornrat, Free vibration analysis of rotating FGP sandwich cylindrical shells with metal-foam core layer, Mech. Adv. Mater. Struct., vol. 30, no. 16, pp. 3318–3331, 2023. DOI: 10.1080/15376494.2022.2073410.

[21] N.K. Gupta, N. Mohamed Sheriff, and R. Velmurugan, Experimental and theoretical studies on buckling of thin spherical shells under axial loads, Int. J. Mech. Sci., vol. 50, no. 3, pp. 422–432, 2008. DOI: 10.1016/j.ijmecsci.2007.10.002.

[22] F. Yin, X. Zhi, F. Fan, W. Wei, and D. Zheng, Blast loads and variability on cylindrical shells under different charge orientations, Sci. Rep., vol. 13, no. 1, p. 6719, 2023. DOI: 10.1038/s41598-023-30785-8.

[23] N.D. Dat, V.T.T. Anh, and N.D. Duc, Vibration characteristics and shape optimization of FG-GPLRC cylindrical shell with magneto-electro-elastic face sheets, Acta Mech., vol. 234, no. 10, pp. 4749–4773, 2023. DOI: 10.1007/s00707-023-03620-4.

[24] A. Karakoti, S. Pandey, and V.R. Kar, Nonlinear transient analysis of porous P-FGM and S-FGM sandwich plates and shell panels under blast loading and thermal environment, Thin. Walled Struct., vol. 173, p. 108985, 2022. DOI: 10.1016/j.tws.2022.108985.

[25] E. Carrera, Theories and finite elements for multilayered plates and shells: a unified compact formulation with numerical assessment and benchmarking, ARCO, vol. 10, no. 3, pp. 215–296, 2003. DOI: 10.1007/BF02736224.

[26] E. Carrera, and V.V. Zozulya, Carrera unified formulation (CUF) for the micropolar plates and shells. I. Higher order theory, Mech. Adv. Mater. Struct., vol. 29, no. 6, pp. 773–795, 2022. DOI: 10.1080/15376494.2020.1793241.

[27] E. Carrera, and V.V. Zozulya, Carrera unified formulation for the micropolar plates, Mech. Adv. Mater. Struct., vol. 29, no. 22, pp. 3163–3186, 2022. DOI: 10.1080/15376494.2021.1889726.

[28] E. Carrera, and V.V. Zozulya, Carrera unified formulation (CUF) for the composite plates and shells of revolution. Layer-wise models, Compos. Struct., vol. 334, p. 117936, 2024. DOI: 10.1016/j.compstruct.2024.117936.

[29] A. Robaldo, E. Carrera, and A. Benjeddou, A unified formulation for finite element analysis of piezoelectric adaptive plates, Comput. Struct., vol. 84, no. 22–23, pp. 1494–1505, 2006. DOI: 10.1016/j.compstruc.2006.01.029.

[30] V.V. Zozulya, and E. Carrera, Carrera unified formulation (CUF) for the micropolar plates and shells. III. Classical models, Mech. Adv. Mater. Struct., vol. 29, no. 27, pp. 6336–6360, 2022. DOI: 10.1080/15376494.2021.1975855.

[31] E. Carrera, and V.V. Zozulya, Carrera unified formulation (CUF) for the shells of revolution. Numerical evaluation, Mech. Adv. Mater. Struct., vol. 31, no. 7, pp. 1597–1619, 2024. DOI: 10.1080/15376494.2022.2140234.

[32] E. Carrera, and V.V. Zozulya, Carrera Unified Formulation (CUF) for the Composite Shells of Revolution. Equivalent Single Layer Models, Mech. Adv. Mater. Struct., vol. 31, no. 1, pp. 22–44, 2024. DOI: 10.1080/15376494.2023.2218380.

[33] Z. Wang, T. Zhou, S. Zhang, C. Sun, J. Li, and J. Tan, Bo-LSTM based cross-sectional profile sequence progressive prediction method for metal tube rotate draw bending, Adv. Eng. Inf., vol. 58, p. 102152, 2023. DOI: 10.1016/j.aei.2023.102152.

[34] J. Li, Z. Wang, S. Zhang, Y. Lin, L. Jiang, and J. Tan, Task incremental learning-driven digital-twin predictive modeling for customized metal forming product manufacturing process, Rob. Comput. Integr. Manuf., vol. 85, p. 102647, 2024. DOI: 10.1016/j.rcim.2023.102647.

[35] R.-S. Chen, H.-Y. Zhang, X.-K. Hao, H.-X. Yu, T. Shi, H.-S. Zhou, R.-B. Wang, Z.-F. Zhao, and P. Wang, Experimental study on ultimate bearing capacity of short thin-walled steel tubes reinforced with high-ductility concrete, Structures, vol. 68, p. 107109, 2024. DOI: 10.1016/j.istruc.2024.107109.

[36] Y. Guo, L. Wang, Z. Zhang, J. Cao, X. Xia, and Y. Liu, Integrated modeling for retired mechanical product genes in remanufacturing: a knowledge graph-based approach, Adv. Eng. Inf., vol. 59, p. 102254, 2024. DOI: 10.1016/j.aei.2023.102254.

[37] X. Long, K. Chong, Y. Su, C. Chang, and L. Zhao, Meso-scale low-cycle fatigue damage of polycrystalline nickel-based alloy by crystal plasticity finite element method, Int. J. Fatigue, vol. 175, p. 107778, 2023. DOI: 10.1016/j.ijfatigue.2023.107778.

[38] D. Lu, X. Zhou, X. Du, and G. Wang, 3D dynamic elastoplastic constitutive model of concrete within the framework of rate-dependent consistency condition, J. Eng. Mech., vol. 146, no. 11, p. 04020124, 2020. DOI: 10.1061/(ASCE)EM.1943-7889.0001854.

[39] J. Cao, J. Du, H. Zhang, H. He, C. Bao, and Y. Liu, Mechanical properties of multi-bolted glulam connection with slotted-in steel plates, Constr. Build. Mater., vol. 433, p. 136608, 2024. DOI: 10.1016/j.conbuildmat.2024.136608.

[40] Y. Wang, and O. Sigmund, Multi-material topology optimization for maximizing structural stability under thermo-mechanical loading, Comput. Methods Appl. Mech. Eng., vol. 407, p. 115938, 2023. DOI: 10.1016/j.cma.2023.115938.

[41] H. Khorshidi, C. Zhang, E. Najafi, and M. Ghasemi, Fresh, mechanical and microstructural properties of alkali-activated composites incorporating nanomaterials: a comprehensive review, J. Cleaner Prod., vol. 384, p. 135390, 2023. DOI: 10.1016/j.jclepro.2022.135390.

[42] W. Zhang, S. Kang, X. Liu, B. Lin, and Y. Huang, Experimental study of a composite beam externally bonded with a carbon fiber-reinforced plastic plate, J. Build. Eng., vol. 71, p. 106522, 2023. DOI: 10.1016/j.jobe.2023.106522.

[43] P. Mehrabi, M. Shariati, K. Kabirifar, M. Jarrah, H. Rasekh, N.T. Trung, A. Shariati, and S. Jahandari, Effect of pumice powder and nano-clay on the strength and permeability of fiber-reinforced pervious concrete incorporating recycled concrete aggregate, Constr. Build. Mater., vol. 287, p. 122652, 2021. DOI: 10.1016/j.conbuildmat.2021.122652.

[44] E. Taheri, A. Firouzianhaji, N. Usefi, P. Mehrabi, H. Ronagh, and B. Samali, Investigation of a method for strengthening perforated cold-formed steel profiles under compression loads, Appl. Sci., vol. 9, no. 23, p. 5085, 2019. DOI: 10.3390/app9235085.

[45] B. Liu, H. Yang, and S. Karekal, Effect of water content on argillization of mudstone during the tunnelling process, Rock Mech. Rock Eng., vol. 53, no. 2, pp. 799–813, 2020. DOI: 10.1007/s00603-019-01947-w.

[46] H. Yang, C. Chen, J. Ni, and S. Karekal, A hyperspectral evaluation approach for quantifying salt-induced weathering of sandstone, Sci. Total Environ., vol. 885, p. 163886, 2023. DOI: 10.1016/j.scitotenv.2023.163886.

[47] H. Yang, J. Ni, C. Chen, and Y. Chen, Weathering assessment approach for building sandstone using hyperspectral imaging technique, Herit. Sci., vol. 11, no. 1, pp. 70, 2023. DOI: 10.1186/s40494-023-00914-7.

[48] H. Yang, K. Song, and J. Zhou, Automated recognition model of geomechanical information based on operational data of tunneling boring machines, Rock Mech. Rock Eng., vol. 55, no. 3, pp. 1499–1516, 2022. DOI: 10.1007/s00603-021-02723-5.

[49] C. Chen, H. Yang, K. Song, D. Liang, Y. Zhang, and J. Ni, Dissolution feature differences of carbonate rock within hydro-fluctuation belt located in the three gorges reservoir area, Eng. Geol., vol. 327, p. 107362, 2023. DOI: 10.1016/j.enggeo.2023.107362.

[50] K. Song, H. Yang, D. Liang, L. Chen, and M. Jaboyedoff, Step-like displacement prediction and failure mechanism analysis of slow-moving reservoir landslide, J. Hydrol., vol. 628, p. 130588, 2024. DOI: 10.1016/j.jhydrol.2023.130588.

[51] D. Hu, H. Sun, P. Mehrabi, Y.A. Ali, and M. Al-Razgan, Application of artificial intelligence technique in optimization and prediction of the stability of the walls against wind loads in building design, Mech. Adv. Mater. Struct., vol. 31, no. 19, pp. 4755–4772, 2024. DOI: 10.1080/15376494.2023.2206208.

[52] J. Wu, Y. Yang, P. Mehrabi, and E.A. Nasr, Efficient machine-learning algorithm applied to predict the transient shock reaction of the elastic structure partially rested on the viscoelastic substrate, Mech. Adv. Mater. Struct., vol. 31, no. 16, pp. 3700–3724, 2024. DOI: 10.1080/15376494.2023.2183289.

[53] S. Han, D. Zheng, B. Mehdizadeh, E.A. Nasr, M.U. Khandaker, M. Salman, and P. Mehrabi, Sustainable design of self-consolidating green concrete with partial replacements for cement through neural-network and fuzzy technique, Sustainability, vol. 15, no. 6, p. 4752, 2023. DOI: 10.3390/su15064752.

[54] S. Han, Z. Zhu, M. Mortazavi, A.M. El-Sherbeeny, and P. Mehrabi, Analytical assessment of the structural behavior of a specific composite floor system at elevated temperatures using a newly developed hybrid intelligence method, Buildings, vol. 13, no. 3, p. 799, 2023. DOI: 10.3390/buildings13030799.

[55] A. Firouzianhaji, N. Usefi, B. Samali, and P. Mehrabi, Shake table testing of standard cold-formed steel storage rack, Appl. Sci., vol. 11, no. 4, p. 1821, 2021. DOI: 10.3390/app11041821.

[56] P. Mehrabi, S. Honarbari, S. Rafiei, S. Jahandari, and M. Alizadeh Bidgoli, Seismic response prediction of FRC rectangular columns using intelligent fuzzy-based hybrid metaheuristic techniques, J. Ambient Intell. Humaniz. Comput., vol. 12, no. 11, pp. 10105–10123, 2021. DOI: 10.1007/s12652-020-02776-4.

[57] E. Taheri, P. Mehrabi, S. Rafiei, and B. Samali, Numerical evaluation of the upright columns with partial reinforcement along with the utilisation of neural networks with combining feature-selection method to predict the load and displacement, Appl. Sci., vol. 11, no. 22, p. 11056, 2021. DOI: 10.3390/app112211056.

[58] J. Liu, M. Mohammadi, Y. Zhan, P. Zheng, M. Rashidi, and P. Mehrabi, Utilizing artificial intelligence to predict the superplasticizer demand of self-consolidating concrete incorporating pumice, slag, and fly ash powders, Materials, vol. 14, no. 22, p. 6792, 2021. DOI: 10.3390/ma14226792.

[59] Y. Feng, M. Mohammadi, L. Wang, M. Rashidi, and P. Mehrabi, Application of artificial intelligence to evaluate the fresh properties of self-consolidating concrete, Materials, vol. 14, no. 17, p. 4885, 2021. DOI: 10.3390/ma14174885.

[60] E. Taheri, A. Firouzianhaji, P. Mehrabi, B. Vosough Hosseini, and B. Samali, Experimental and numerical investigation of a method for strengthening cold-formed steel profiles in bending, Appl. Sci., vol. 10, no. 11, p. 3855, 2020. DOI: 10.3390/app10113855.

[61] Y. Qiu, and J. Wang, A Machine Learning Approach to Credit Card Customer Segmentation for Economic Stability. In Proceedings of the 4th International Conference on Economic Management and Big Data Applications, ICEMBDA 2023, October 27–29, 2023, Tianjin, China. 2024.

[62] Y. Qiu, Estimation of tail risk measures in finance: Approaches to extreme value mixture modeling. Johns Hopkins University, Diss. Johns Hopkins University, 2019.

[63] K.Q. Tran, T.-D. Hoang, J. Lee, and H. Nguyen-Xuan, Three novel computational modeling frameworks of 3D-printed graphene platelets reinforced functionally graded triply periodic minimal surface (GPLR-FG-TPMS) plates, Appl. Math. Modell., vol. 126, no. February, pp. 667–697, 2024. DOI: 10.1016/j.apm.2023.10.043.

[64] D.-L. Shi, X.-Q. Feng, Y.Y. Huang, K.-C. Hwang, and H. Gao, The effect of nanotube waviness and agglomeration on the elastic property of carbon nanotube-reinforced composites, J. Eng. Mater. Technol., vol. 126, no. 3, pp. 250–257, 2004. DOI: 10.1115/1.1751182.

[65] B. Szabó, A. Düster, and E. Rank, The P-version of the finite element method, Encyclopedia Comput. Mech., 2004. https://doi.org/10.1002/0470091355.ecm003g

[66] E. Carrera, A.G. de Miguel, and A. Pagani, Hierarchical theories of structures based on legendre polynomial expansions with finite element applications, Int. J. Mech. Sci., vol. 120, pp. 286–300, 2017. DOI: 10.1016/j.ijmecsci.2016.10.009.

[67] Y. Yan, E. Carrera, A.G. de Miguel, A. Pagani, and Q.-W. Ren, Meshless analysis of metallic and composite beam structures by advanced hierarchical models with layer-wise capabilities, Compos. Struct., vol. 200, pp. 380–395, 2018. DOI: 10.1016/j.compstruct.2018.05.114.

[68] J.N. Reddy, Mechanics of Laminated Composite Plates and Shells: Theory and Analysis, CRC Press, 2003.

[69] J.A. Cottrell, T.J.R. Hughes, and Y. Bazilevs, Isogeometric Analysis: Toward Integration of CAD and FEA, John Wiley & Sons, 2009.

[70] T.J.R. Hughes, J.A. Cottrell, and Y. Bazilevs, Isogeometric analysis: CAD, finite elements, NURBS, exact geometry and mesh refinement, Comput. Methods Appl. Mech. Eng., vol. 194, no. 39–41, pp. 4135–4195, 2005. DOI: 10.1016/j.cma.2004.10.008.

[71] A. Toghroli, P. Mehrabi, M. Shariati, N.T. Trung, S. Jahandari, and H. Rasekh, Evaluating the use of recycled concrete aggregate and pozzolanic additives in fiber-reinforced pervious concrete with industrial and recycled fibers, Constr. Build. Mater., vol. 252, p. 118997, 2020. DOI: 10.1016/j.conbuildmat.2020.118997.

[72] F. Durbin, Numerical inversion of laplace transforms: an efficient improvement to Dubner and Abate's method, Comput. J., vol. 17, no. 4, pp. 371–376, 1974. DOI: 10.1093/comjnl/17.4.371.

[73] M. Dan, A. Pagani, and E. Carrera, Free vibration analysis of simply supported beams with solid and thin-walled cross-sections using higher-order theories based on displacement variables, Thin. Walled Struct., vol. 98, pp. 478–495, 2016. DOI: 10.1016/j.tws.2015.10.012.

[74] A. Pagani, M. Boscolo, J.R. Banerjee, and E. Carrera, Exact dynamic stiffness elements based on one-dimensional higher-order theories for free vibration analysis of solid and thin-walled structures, J. Sound Vib., vol. 332, no. 23, pp. 6104–6127, 2013. DOI: 10.1016/j.jsv.2013.06.023.

Appendix A

A.1. Definition of n_A and n_S

The following are the power indexes, n_A and n_S, respectively [74].

$$n_A = \frac{\rho_{\max} - \frac{M}{\rho_s h}}{\frac{M}{\rho_s h} - \rho_{\max}(1-\rho_0)}, \tag{A1-1a}$$

$$\frac{M}{\rho_s h} = \int_0^1 \frac{2}{\pi} \frac{\rho_{\max}\left[1-\rho_0+\rho_0(1-\phi)^{n_S}\right]}{\sqrt{1-\phi^2}} d\phi, \tag{A1-1b}$$

with $\phi = \cos\left(\frac{\pi z}{h}\right)$ and M refers to the total mass per surface area of the TPMS substrate layer.

A.2. Definition of effective properties

The isotropic mechanical characteristics of CNTR material may be computed using the effective material properties of agglomeration ($aggl$) and non-agglomeration ($non-aggl$) areas, in accordance with the Eshelby–Mori–Tanaka (EMT) micro-mechanical scheme.

$$E_s = \frac{9K_sG_s}{3K_s+G_s}, \nu_s = \frac{3K_s-2G_s}{6K_s+2G_s}, \tag{A2-1a}$$

$$K_s = K_{non-aggl}\left(1+\frac{\mu\left(\frac{K_{aggl}}{K_{non-aggl}}-1\right)}{1+\alpha(1-\mu)\left(\frac{K_{aggl}}{K_{non-aggl}}-1\right)}\right), \tag{A2-1b}$$

$$G_s = G_{non-aggl}\left(1+\frac{\mu\left(\frac{G_{aggl}}{G_{non-aggl}}-1\right)}{1+\beta(1-\mu)\left(\frac{G_{aggl}}{G_{non-aggl}}-1\right)}\right), \tag{A2-1c}$$

where

$$\alpha = \frac{1+\nu_{non-aggl}}{3(1-\nu_{non-aggl})}, \beta = \frac{2(4-5\nu_{non-aggl})}{15(1-\nu_{non-aggl})}, \tag{A2-2a}$$

$$\nu_{non-aggl} = \frac{3K_{non-aggl}-2G_{non-aggl}}{6K_{non-aggl}+2G_{non-aggl}}. \tag{A2-2b}$$

Besides, the mechanical properties of these regions can be calculated *via*

$$\begin{aligned} K_{aggl} &= K_m + \frac{\mathrm{v}_r\zeta(\delta_r - 3K_m\alpha_r)}{3(\xi-\mathrm{v}_r\zeta+\mathrm{v}_r\zeta\alpha_r)}, \\ G_{aggl} &= G_m + \frac{\mathrm{v}_r\zeta(\eta_r - 2G_m\beta_r)}{2(\xi-\mathrm{v}_r\zeta+\mathrm{v}_r\zeta\beta_r)}, \end{aligned} \tag{A2-3a}$$

$$K_{non-aggl} = K_m + \frac{\mathrm{v}_r(1-\eta)(\delta_r-3K_m\alpha_r)}{3(1-\xi-\mathrm{v}_r(1-\eta)+\mathrm{v}_r(1-\eta)\alpha_r)}, \tag{A2-3b}$$

$$G_{non-aggl} = G_m + \frac{\mathrm{v}_r(1-\eta)(\eta_r-2G_m\beta_r)}{2(1-\xi-\mathrm{v}_r(1-\eta)+\mathrm{v}_r(1-\eta)\beta_r)}. \tag{A2-3c}$$

where

$$\alpha_r = \frac{3K_m+3G_m+k_r-l_r}{3G_m+3k_r}, \tag{A2-4a}$$

$$\beta_r = \frac{4G_m + 2k_r + l_r}{15G_m + 15k_r} + \frac{4G_m}{5G_m + 5p_r} + \frac{2G_m(3K_m + G_m) + 2G_m(3K_m + 7G_m)}{5G_m(3K_m + G_m) + 5m_r(3K_m + 7G_m)}, \quad \text{(A2-4b)}$$

$$\delta_r = \frac{(3K_m + 2G_m - l_r)(2k_r + l_r)}{3G_m + 3k_r} + \frac{1}{3}(n_r + 2l_r), \quad \text{(A2-4c)}$$

$$\eta_r = \frac{8G_m p_r}{5G_m + 5p_r} + \frac{8G_m m_r(3K_m + 4G_m)}{15K_m(G_m + m_r) + 5G_m(7m_r + G_m)} + \frac{2(2G_m + l_r)(k_r - l_r)}{15G_m + 15k_r} + \frac{2}{15}(n_r - l_r). \quad \text{(A2-4d)}$$

where $K_m = E_m/[3(1-2\nu_m)]$, and $G_m = E_m/[2(1+\nu_m)]$ stand for Hill's elastic moduli of the reinforcement component, and k_r, l_r, m_r, n_r, and p_r for the Young's modulus and Poisson's ratio of the composite matrix, respectively.